This is the peer-reviewed, final accepted version for American Mineralogist, published by the Mineralogical Society of America.
The published version is subject to change. Cite as Authors (Year) Title. American Mineralogist, in press.
DOI: https://doi.org/10.2138/am-2022-8030. http://www.minsocam.org/

Revision 1

In situ chemical and isotopic analyses and element mapping of multiple-generation pyrite: evidence of episodic gold mobilization and deposition for the Qiucun epithermal gold deposit in Southeast China

Ying Ma[1,2], Shao-Yong Jiang[1*], Hartwig E. Frimmel[2,3], and Lü-Yun Zhu[1,4]

1. *State Key Laboratory of Geological Processes and Mineral Resources, School of Earth Resources, Collaborative Innovation Center for Exploration of Strategic Mineral Resources, China University of Geosciences, Wuhan 430074, P.R. China*

2. *Bavarian Georesources Center, Institute of Geography and Geology, University of Würzburg, Am Hubland, Würzburg 97074, Germany*

3. *Department of Geological Sciences, University of Cape Town, Rondebosch 7700, South Aferica*

4. *College of Zijin Mining, Fuzhou University, Fuzhou 350108, P.R. China*

* *Corresponding author*: shyjiang@cug.edu.cn (Prof. Dr. S.-Y. Jiang).

ABSTRACT

Gold deposits are often the result of complex mineralization and remobilization processes. Interpretation of bulk geochemical and sulfur isotope data of the gold deposits is frequently hampered by complex zoning in pyrite, which calls for *in situ* determination of geochemical and sulfur isotope composition of sulfide minerals. The Qiucun deposit is a good representative of epithermal gold deposit in the Mesozoic Coastal Volcanic Belt of southeastern China. It represents a complex mineralization history, comprising three hydrothermal stages: (I) early stage of

pyrite-quartz-chalcedony, (II) main ore stage of quartz-polymetallic sulfide, and (III) post-ore stage of quartz-carbonate. Detailed backscattered electron imaging (BSE), *in situ* trace element and sulfur isotope analyses using laser ablation-inductively coupled plasma-mass spectrometry (LA-ICP-MS) and LA-multicollector (MC)-ICP-MS were applied to reveal the gold mineralization and remobilization history of this deposit. Four texturally distinct generations of pyrite were identified, all of which host invisible gold: Py_{1a} and Py_{1b} in Stage I and Py_{2a} and Py_{2b} in Stage II. A detailed study of the texture, chemistry, and sulfur isotopic composition as well as hydrothermal evolution of auriferous pyrite from the Qiucun deposit revealed the behavior of gold in the course of pyrite evolution. Pyrite of stages I and II contains invisible gold whereas later-stage visible native gold and re-enrichment in invisible is associated with alteration rims around the primary pyrite grains. Py_{1a} is rich in silicate inclusions, enriched in Co and Ni, and depleted in As and Au relative to later pyrite generations. This redistribution is attributed to alteration of biotite in the sub-volcanic host rocks that effectively destabilized gold in the ore fluid during Py_{1a} deposition. Py_{1b} and Py_{2a} show oscillatory zoning with bright bands having elevated As and Au contents. The oscillatory zoning is interpreted to reflect pressure fluctuations and repeated local fluid boiling around the pyrite crystals. These three pyrite generations ($Py_{1a,\ 1b,\ 2a}$) record a narrow range of $\delta^{34}S_{V\text{-}CDT}$ values between -3.6 ‰ and 4.6 ‰, consistent with a magmatic sulfur source. Gold and some trace elements (As, Ag, Sb, Pb, Tl, and Cu) that were initially incorporated into Py_{2a} became partially exsolved and remobilized during the replacement of porous and invisible gold-rich Py_{2b}. This replacement was likely due to coupled dissolution and re-precipitation reactions triggered by oxidation of the mineralizing fluids. Fluid oxidation is further supported by a general decrease trend of $\delta^{34}S_{V\text{-}CDT}$ from Py_{2a} (-3.2 to 4.6 ‰) to Py_{2b} (-15.2 to -2.3 ‰). Lastly, previously formed auriferous pyrite underwent post-mineralization fracturing, causing local pulverization of pyrite. Thus newly created porosity facilitated fluid circulation, hydrothermal alteration of the pyrite, and remobilization of invisible gold, which re-precipitated with pyrite in the form of electrum as small inclusions or as larger grains within

fractures. Our study emphasizes that pressure-driven hydrothermal processes play a vital role in the initial enrichment and re-concentration of gold and some other trace metals during episodic deposition, replacement, and hydrothermal alteration of gold-bearing pyrite in epithermal gold deposits, ultimately forming visible gold and high-grade ore shoots as exemplified by the Qiucun deposit.

Keywords: Pyrite formation and replacement; Sulfur isotopes; Gold remobilization; Epithermal gold mineralization

INTRODUCTION

Large gold deposits may form by multiple gold enrichment events, but it is often hard to clarify whether the last of these events represents remobilized gold from pre-existing mineralization or relates to new gold introduction during a distinct epigenetic event (Large et al. 2009; Haroldson et al. 2018). In many gold deposits, gold shows a bimodal distribution in which refractory gold within pyrite was overprinted by later visible gold as distinct inclusions or filling fractures within the pyrite. The former is either primary in origin or a result of the remobilization of refractory gold. In contrast, the latter is considered to be remobilized invisible gold within fractures of the pyrite (e.g., Morey et al. 2008; Cook et al. 2009; Large et al. 2011). This gold remobilization could lead to secondary gold enrichment and help understand the origin of bonanza zones within gold deposits, which considerably enhance bulk gold grade.

Pyrite occurs in various crustal environments and is one of the most important host minerals for gold. Gold incorporated in pyrite as solid solution (Au^{+}) and/or submicron particles (Au^{0}) is referred to as invisible (refractory) gold (Gopon et al. 2019). This type of gold, which can reach concentrations from tens of ppb to >1 wt.% (Deditius et al. 2014), is generally thought to be a primary precipitation feature (e.g., Reich et al. 2005; Velásquez et al. 2014). However, the physico-chemical controls on this type of gold mineralization are still under debate, with fluid

temperature, pH, oxidation state, and sulfur fugacity all playing potentially important roles (Gregory et al. 2019).

The texture and chemistry of pyrite have been used extensively in unraveling the genesis and evolution of many ore deposits (Franchini et al. 2015; Sykora et al. 2018). The texture and morphology of pyrite can reflect replacement or dissolution and can also be used to distinguish between supersaturation, near-equilibrium crystallization, or recrystallization. The trace element distribution in pyrite and included nanoparticles may reveal changes in temperature, pH, oxidation state, source and composition of the ore fluid (e.g., Deditius et al. 2011; Velásquez et al. 2014). The sulfur isotope ratios of pyrite can provide useful information on the fluid source and decipher physicochemical conditions during precipitation (Ohmoto 1972). However, interpretation of geochemical and sulfur isotope data is far from straightforward because gold-bearing pyrite usually resulted from multiple stages of overgrowths. Thus, geochemical and sulfur isotope data derived using bulk analysis represent a mixed-signal, from which no definite conclusion can be drawn. *In situ* determination of trace element concentration, in combination with sulfur isotope analysis, has been used more and more in the past few years, and the high spatial resolution of these techniques provides a promising tool to reveal the complex overgrowth in single grains and to reveal the detailed episodic gold deposition and remobilization history in gold deposits (Morey et al. 2008; Cook et al. 2009; Velásquez et al. 2014; Gregory et al. 2019).

The Mesozoic Coastal Volcanic Belt in southeastern China is one of the most important mineral provinces in China, hosting many epithermal gold deposits, with a total gold reserve of over 480 t, including the world-class Zijinshan gold deposit (323 t Au, average grade: 0.5 g/t, Zhong et al. 2017; White et al. 2019). This contribution reports on the mineralogical distribution of gold in the Qiucun epithermal deposit in the Dehua goldfield of southeastern China (Fig. 1). There, gold occurs as both visible gold and as Au-rich pyritic refractory ore. A fluid inclusion study by Ni et al. (2018) suggested that mineralization took place at 180°–250 °C, and the ore fluid was dilute (<2.6 wt.%

NaCl equiv.), near-neutral, CO_2-bearing, and formed during boiling. Liu (2018) proposed that the mineralizing fluid consisted of a mixture of magmatic and meteoric components based on stable isotope data. Despite the many studies on the mine geology, fluid inclusions, and stable isotopes, the mineralogy and mineral paragenesis of this deposit remains poorly understood.

Previous studies showed that the auriferous pyrite in the Dehua goldfield is commonly zoned (Zhang et al. 2018) with regard to its chemical and S isotopic composition. Consequently, traditional whole-grain analyses must be considered as "average compositions" of different zones. The situation is even further complicated by minute mineral inclusions in the pyrite. In this study, we used *in-situ* LA-ICP-MS trace element spot and map analyses to investigate the textural and crystallo-chemical relationships between gold and the associated metals in the hosting pyrite. A link between multistage pyrite formation and initial gold deposition is established, and the effect of pyrite deformation on the remobilization of gold in the epithermal environment is described. Lastly, we conducted *in-situ* LA-MC-ICP-MS sulfur isotope analysis of texturally complex pyrite to examine microscopic variations of sulfur isotope compositions in the ore-forming processes. The results are used to track the sulfur source and the changes in physico-chemical conditions during ore formation.

GEOLOGICAL BACKGROUND

Regional geology

The South China Block (SCB) resulted from the amalgamation of the Cathaysia and Yangtze blocks during Neoproterozoic times (Fig. 1a; Wang and Li 2003). After two intraplate orogenies during the Early Paleozoic and Early Mesozoic (Shu et al. 2015), a western Pacific continental margin formed in the SCB in the Late Mesozoic, marking a change from Tethyan to Pacific tectonism (Zhou et al. 2006). Since the Early Jurassic, the westward subduction of the paleo-Pacific plate beneath the SCB has induced large-scale lithospheric extension and intensive magmatism,

which produced the Mesozoic Coastal Volcanic Belt in the southeastern margin of the SCB (Fig. 1b; Zhou et al. 2006).

The Dehua goldfield represents a typical example of mineralization within the Coastal Volcanic Belt (Fig. 1b; Ma et al. 2021a). Neoproterozoic metamorphic basement, Paleozoic to Triassic clastic sedimentary rocks, and Jurassic continental clastic and volcanic rocks are the major rock types in the area (Fig. 2a). The Jurassic strata of the Dehua area are subdivided, in ascending order, into the Lishan Formation sandstone, the Changlin Formation sandstone, and the comparatively widespread Nanyuan Formation (Fig. 2a). The latter is composed of Late Jurassic, 169–157 Ma dacitic to rhyolitic tuff, rhyolite, and tuffaceous sandstone (Li et al. 2020). These volcano-sedimentary rocks host the epithermal gold deposits (e.g., Dongyang, Qiucun, Ancun, Lingtouping, and Chunhu) in the region (Fig. 2b).

The sedimentary units of the Dehua area were intruded by widespread Silurian and subordinate Triassic and Jurassic to Cretaceous granitic magmas (Fig. 2a), which were generated by partial melting of the Proterozoic basement rocks (Shu et al. 2015). The main geologic structures of the Dehua goldfield include a series of NE-, NW-, and nearly N-S-striking faults (Fig. 2a). The NE- and NW-striking faults of Mesozoic age are two sets of the most important structures, spatially controlling the emplacement of Mesozoic granites and the distribution of gold deposits (Fig. 2a).

Geology of the Qiucun gold deposit

The Qiucun deposit is situated in the northern portion of the Dehua goldfield (Fig. 2a). It is hosted mainly by sub-volcanic rocks of the Nanyuan Formation, subordinately by sandstone of the Changlin Formation (Figs. 2b-c). The exposed intrusive rocks are mainly Silurian quartz diorite, Jurassic rhyolite porphyry and diorite dikes (Figs. 2b-c). The major structures in the Qiucun area are NW-striking normal and NE-striking reverse faults (Fig. 2b). The latter are represented by the so-called F_1, F_2, F_3, F_7, F_{11}, F_{12}, and F_{13}, which are largely filled by in places auriferous quartz veins and diorite dikes, striking 45°-60° and dipping 45°-89° to the southeast (Figs. 2b-c; Fan 2015). The

NW-striking normal faults are younger than the mineralization (locally referred to as the F_{19}, F_{20}, F_{301}; Fig. 2b) and located in the northeastern and southeastern parts of the deposit.

The Qiucun gold deposit consists of 16 orebodies with a total proven reserve of 10 t Au in 2017 (Huang et al. 2017). The so-called Au_{11} is the largest gold orebody, extending from 940 to 660 m in elevation, dipping to the northwest at 70°, and varying in thickness from 0.6 to 34 m (average 4.0 m), with a Au grade of 4.9 g/t and a strike length of about 310 m (Fig. 2c). Gold is present in economic concentrations (3 to 30 g/t), largely confined to quartz veins and silicified hydrothermal breccias and wall rocks. Wall rock alteration is pervasive and is best developed adjacent to the auriferous quartz veins and breccias. The alteration assemblages consist mainly of quartz, sericite, chlorite, illite, and carbonate, with minor disseminations of pyrite. Higher gold concentrations (locally reaching bonanza grades of 300-500 g/t) predominate at depth, in a zone of postulated high fluid flow rate, repeated hydraulic fracturing, and episodic boiling.

SAMPLING AND ANALYTICAL METHODS

Electron microprobe analysis

Eleven hand-specimen samples (Supplementary Appendix Table A1), representative of mineralization stages I and II, were collected from underground at the 712-m, 742-m, and 802-m levels. Polished thin sections containing sufficient amounts of sulfide minerals and their host rocks were characterized by electron microprobe analysis (EMPA). The EMPA was performed using a JEOL JXA-8230 superprobe housed at the Testing Center of the China Metallurgical Geological Bureau, Shandong. Standards and unknowns were analyzed using a 5-μm beam diameter, an accelerating voltage of 20 kV, and a beam current of 20 nA. Calibration standards used were pyrite for S and Fe, chalcopyrite for Cu, sphalerite for Zn, galena for Pb, and alloy or pure metal for As, Co, Ni, Sb, Ag, and Au. The detection limits for each element were as follows: S (109 ppm), Fe (149 ppm), As (234 ppm), Co (80 ppm), Ni (93 ppm), Sb (361 ppm), Pb (438 ppm), Cu (227 ppm), Au

(818 ppm), Ag (272 ppm), and Zn (299 ppm). The data were reduced using the ZAF correction method.

In situ trace element analysis of pyrite

Trace element concentrations of pyrite were conducted using LA-ICP-MS housed at the Nanjing FocuMs Technology Co. Ltd., China. The analytical instrumentation employed in this study was a Photon Machines Analyte G2 193-nm ArF excimer laser ablation system attached to an Agilent 7700x Quadrupole ICP-MS. The operating conditions and procedures applied to pyrite have been detailed in Gao et al. (2015). Spot analyses were used for individual analyses of various chemical zones as determined by EMPA. Spot ablation was carried out using a spot size of 40 μm at 3.5 J/cm^2 and a 6-Hz repetition rate. Each analysis consisted of a 20 s laser-off period to measure background and a 35-s laser-on period for the analysis. USGS polymetallic sulfide pressed pellet MASS-1 and synthetic basaltic glasses GSE-1G were used for calibration (Wilson et al. 2002). Standard blocks were run after every ten unknown samples. Data reduction was performed offline using ICPDATACAL software (Liu et al. 2008), and the Fe content as determined by EMPA was used as reference for the calculation of trace element concentrations.

Element mapping of pyrite

Quantitative element distribution maps of pyrite grains were generated by LA-ICP-MS in the In Situ Mineral Geochemistry Lab at the Hefei University of Technology, China. Maps were acquired using a Photon Machines Analyte HE 193-nm laser ablation microprobe coupled to an Agilent 7900 Quadrupole ICP-MS. The maps were collected by rastering the laser over the region of interest with 45 s of washout between individual lines. Maps were acquired using a beam diameter of 15 μm with a laser repetition rate of 7 Hz and a scan velocity of 12 μm/s. The raw data were quantified and compiled into maps using the LIMS software package (Wang et al. 2017), with synthetic NIST SRM 610 glass as an external reference material, and Fe as an internal reference, and BHVO-2G glass as monitor for quality control (Jochum et al. 2005; Gourcerol et al. 2018; Kerr et al. 2018; Hastie et al.

2020). Considering the differences in ablation between silicate glasses (NIST 610) and sulfides, it is expected that fractionation limits the accuracy of the quantified data to ~20% (Wohlgemuth-Ueberwasser and Jochum 2015).

In situ sulfur isotope analysis

Polished thin sections analyzed for LA-ICP-MS trace element spot analysis were repolished and used for *in situ* sulfur isotope analysis. *In situ* S isotope analyses of pyrite were performed using a Nu Plasma II MC-ICP-MS together with a Resonetics-S155 193-nm laser ablation system housed at the GPMR, China University of Geosciences, Wuhan. The analytical methods and operating procedures follow the protocols described by Zhu et al. (2016). The diameter of the laser beam was 33 μm with a repetition rate of 8 Hz and an energy fluency of 3 J/cm^2. An in-house pyrite standard named WS-1 ($\delta^{34}S_{VCDT}$ = 1.1‰; Zhu et al. 2016) was used to correct the instrumental mass bias. The analytical precision is about 0.1‰.

RESULTS

Mineralization stages and multiple generations of pyrite

Three mineralization stages are recognized based on field and petrographic observations (Figs. 3-6). Low-grade Stage I takes the form of fine- to medium-grained gray quartz-chalcedony with minor colloform and vuggy textures (Figs. 3a-c). This stage also includes intergrowth of euhedral or subhedral pyrite. These veins were generally altered and overprinted by later hydrothermal fluids. Stage II is marked by fine-grained white to colourless quartz, and abundant aggregates, massive, or isolated crystals of sulfide minerals (Figs 3d-e). The ore minerals include pyrite, sphalerite, chalcopyrite, galena, and electrum. Calcite and lesser amounts of quartz characterize the Stage III (Fig. 3f).

Pyrite is the predominant sulfide mineral in both Stage I and II veins. Petrographic observations and BSE imaging revealed four generations of pyrite (Fig. 5). The dataset of major element

concentrations in pyrite is given in Supplementary Appendix Table A2. Pyrite (Py_1) from Stage I veins consists of two generations: inclusion-rich anhedral cores (Py_{1a}, Figs. 5a-b), which show neither dissolution textures nor the presence of pores, followed by an inclusion-free outer part of a rhythmic alternation of As-rich (As = 1.0-5.7wt. %) and As-poor zones (As = 0.61-0.91 wt. %) (Py_{1b}, Fig. 5b). Concentrations of As are relatively low (<0.45 wt.%), and all Au contents are below the EMPA detection limit of 975 ppm. Mineral inclusions found in Py_{1a} and rare inclusions in Py_{1b} are mainly quartz, rutile, apatite, sericite, chalcopyrite, and galena.

Two distinct generations of pyrite (Py_{2a} and Py_{2b}) are recognized in the Stage II veins. Py_{2a}, with rare or no silicate inclusions, commonly occurs as subhedral to anhedral overgrowth with oscillatory zoning around Py_1 (Figs. 5d-e). It is coarse- (Figs. 5d-e) to fine-grained (Fig. 5f) and its size ranges from 10 μm to 1 mm. The oscillatory zoning is made up of rhythmically alternating thin bright bands in BSE with high As (0.56-4.2 wt. %), and broader, darker bands with low As (bdl-0.40 wt.%) (Figs. 5d-e). Py_{2b} borders Py_{2a} (Figs. 5g-i) and is also present in microfractures of Py_{2a} (Fig. 5g). Py_{2b} is characterized by abundant pores of varying sizes (1-30 μm in diameter), which exhibit no perceptible preferred orientation. Py_{2b} has high concentrations of As (1.3-4.8 wt.%), causing a bright appearance in BSE images. The As-Fe-S ternary diagram (Fig. 7a) and the As vs. S scatterplot of various pyrite generations (Fig. 7b) suggests that As is bound to the structure of pyrite in substitution for sulfur as $Fe(As_XS_{1-X})_2$, corresponding to the arsenian pyrite of the As^{-1} type (Simon et al. 1999). This is confirmed by the flat ^{75}As spectrum in-depth profiles shown in Supplementary Appendix Figure A1, which supports the notion of As being present as a solid solution.

Trace element distribution in pyrite

A total of 112 LA-ICP-MS spot analyses were performed on various generations of pyrite from Qiucun. Representative time-resolved LA-ICP-MS spectra for each pyrite generation recorded during analyses are shown in Supplementary Appendix Figure A1. Analytical results of different generations of pyrite are provided in Table 1 with median and median absolute deviation values. The

full data sets are available in Supplementary Appendix Table A3. The average detection limits obtained in this study are 0.8 ppm Co, 0.6 ppm Ni, 0.4 ppm Cu, 2.2 ppm Zn, 4.2 ppm As, 0.06 ppm Ag, 0.5 ppm Sb, 0.1 ppm Au, 0.05 ppm Bi, and 0.5 ppm Pb.

Py_{1a} contains higher Co (median 27 ppm) and Ni (26 ppm) compared to $Py1_b$. Other elevated trace elements in Py_{1a} include Ag (median 12 ppm), Pb (149 ppm), and Cu (4 ppm). Notably, Py_{1a} has low Au (bdl–2.5 ppm, median 0.28 ppm) and highly variable As (5.9–5649 ppm, median 323 ppm) contents. In sharp contrast (Fig. 10), Py_{1b} has much higher contents of As (median 6828 ppm), but other trace elements are generally very low compared to Py_{1a} (e.g., median 12 ppm Co, 11 ppm Ni, 65 ppm Pb). The maximum Au and Ag contents in Py_{1b} are 64 and 683 ppm, respectively.

The oscillatory-zoned Py_{2a} consists of alternating As-rich and As-poor bands. The As-rich bands contain about an order of magnitude more As (median 5265 ppm) than the As-poor bands (1490 ppm As); similarly, Au (0.60–16 ppm) and Ag (3.1–1621 ppm) are at higher concentrations in these As-rich bands with respect to the As-poor bands (Au = bdl–1.9 ppm, Ag = bdl–216 ppm). Compared to Py_{2a}, Py_{2b} is enriched in Au (median 31 ppm) and As (13084 ppm). Note that the highest Au value (138 ppm) corresponds to the highest As content of 21879 ppm.

Trace element mapping of pyrite

LA-ICP-MS mapping was performed on three representative pyrite grains: (i) a pyrite grain representing Py_{1a} and Py_{1b} from Stage I (Fig. 10); (ii) a typical oscillatory-zoned Py_{2a} grain from Stage II (Fig. 11); and (iii) a selected area containing Py_{2a} and Py_{2b} from Stage II (Fig. 12).

Figure 10 highlights two generations of a selected Py_1 grain: the porous and inclusion-rich core (Py_{1a}) has elevated Co, Ni, Ag, Pb, and Sb, whereas the overgrowth (Py_{1b}) has relatively high concentrations of Au and As compared to Py_{1a}. This map also confirms a positive correlation between As and Cu in Py_{1b}. The element map of one selected Py_{2a} grain shows that the distributions of Au, As, Ag, Sb, and Tl correlate with the regular and continuous oscillatory zoning pattern displayed by the BSE image (Fig. 11). Zoning is sharply defined and is clearly visible as alternating

This is the peer-reviewed, final accepted version for American Mineralogist, published by the Mineralogical Society of America.
The published version is subject to change. Cite as Authors (Year) Title. American Mineralogist, in press.
DOI: https://doi.org/10.2138/am-2022-8030. http://www.minsocam.org/

broad bands of color. The bright zones are enriched in Au, As, Ag, Sb, and Tl compared to the darker bands, and these elements reach their highest concentrations in a fracture zone of the analyzed Py_{2a} grain, which was corroded by later hydrothermal fluids. Cobalt and Ni display very weak zonation, in which they are higher in the grain cores. Figure 12 indicates two generations of a selected pyrite grain from Stage II: the core (Py_{2a}) with apparent oscillatory zoning, whereas the thin outer rim (Py_{2b}) is enriched in Au, As, Ag, Sb, Tl, and Cu.

In situ sulfur isotope data

The *in situ* sulfur isotope compositions for the different pyrite generations are presented in Supplementary Appendix Table A4 and shown in Figure 13. In Stage I, 13 analyses of Py_{1a} grains yielded a relatively restricted $\delta^{34}S$ range of -2.1 to 2.1 ‰ with a mean value of -0.3 ‰, and 14 analyses of Py_{1b} grains gave a similar $\delta^{34}S$ range of -3.6 to 1.3 ‰ (mean = -0.4 ‰). For Stage II, the $\delta^{34}S$ values of Py_{2a} range from -3.2 to 4.6 ‰ (mean = 0.7 ‰, n = 39), which are significantly higher than those of Py_{2b} with a range between -15.2 and -2.3‰ (mean = -7.3 ‰, n = 18).

DISCUSSION

Pyrite formation and primary gold precipitation

***Py_{1a}*:** Most Py_1 grains are composite grains with trace element-rich rims (Py_{1b}) and relatively trace element-poor cores (Py_{1a}) as highlighted by trace element images determined by LA-ICP-MS (Fig. 10). Overall, Py_{1a} grains are enriched in Co and Ni and depleted in As and Au compared to Py_{1b} (Fig. 8). The solubility of Co and Ni as chloride complexes in hydrothermal fluids is strongly positively correlated to temperature; for example, a decrease in temperature from 300° to 200°C would cause a decrease in Co solubility by over two orders of magnitude (Migdisov et al. 2011). Deditius et al. (2014) established an exponential relation of As content in pyrite with temperature as

$$C_{As} = 0.4785 \times e^{-0.0143T}$$

where C_{As} is As content in mole percent (mol%) and T is temperature (°C). Based on this equation, calculated concentrations of As increase from ~1000 ppm at 400°C to ~20000 ppm at 200°C. Therefore, the variations in Co, Ni, and As may suggest that Py_{1a} grains at Qiucun crystallized at higher temperatures than later pyrite generations. In addition, as shown in Figure 10, the region with high Co and Ni concentrations matches with the dark area (i.e., silicate inclusion-rich) on the BSE image; the silicate inclusions may also account for the high Co and Ni contents in Py_{1a}. Biotite phenocrysts in sub-volcanic host rocks at Qiucun were altered to chlorite and minor rutile. Py_{1a} crystallized near or around the altered biotite (Supplementary Appendix Fig. S2), which contains abundant rutile inclusions, indicating that this alteration preceded of Py_{1a} precipitation. Sulfur was introduced via auriferous fluids, and that the chloritization of biotite provided the iron according to the reaction:

$$4KMgFe_2AlSi_3O_{10}(OH)_2\ (\textit{biotite}) + 4H_2S + O_2 + 4H^+ \rightarrow 2Mg_2Fe_3Al_2Si_3O_{10}(OH)_8\ (\textit{chlorite})$$
$$+ 2FeS_2\ (\textit{pyrite}) + 6SiO_2 + 2H_2O + 4K^+$$

Ti dissolved from biotite quickly precipitated as rutile in and around the altered biotite. Other minerals that make up the alteration paragenesis of sub-volcanic rocks also occur as inclusions in Py_{1a}, which also supports the hypothesis that Py_{1a} was formed via fluid-wall rock interaction. The formation of open space during the replacement of biotite by pyrite can be explained by considering the different densities of these minerals (biotite = 3.09 g/cm^3; pyrite = 5.01 g/cm^3). Assuming that all Fe in pyrite is derived from biotite, the molar volume of the resulting pyrite will be significantly lower than that of biotite. This process may also explain the presence of abundant silicate inclusions in Py_{1a}.

Gold in Py_{1a}: Py_{1a} contains minor amounts of invisible gold (~2.5 ppm), which precipitated contemporaneously to the very first pyrite generation in the vein stock and wall rock. Sulfur isotope ratios ($\delta^{34}S$ = -2.1 to 2.1 ‰) and the absence of sulfates and hematite suggest that H_2S was the predominant sulfur species in the ore fluid during pyrite formation; therefore, $AuHS_2^-$ is likely to

have been the major gold-transporting complex (Ohmoto 1972). As discussed earlier, Py_{1a} formed at the expense of biotite. Thus, the destabilization of gold bisulfide complexes due to loss of H_2S from the ore fluid during sulfidation of the wall rocks was the most likely mechanism for gold deposition (Williams-Jones et al. 2009). The time-invariant trace of the spot analysis and the positive correlation between As and Au indicate that Au and As are most likely contained as solid solution or as nanoparticles in Py_{1a} rather than as inclusions of free gold (Fig. 7a; Reich et al. 2005; Gregory et al. 2016).

Py_{1b} and Py_{2a}: The rims of Py_1 (Py_{1b}) are significantly enriched in As, Au, and Cu compared to their cores (Fig. 10). Py_{1b} has delicate banded textures related to elevated trace element concentrations, and many of the Py_{1b} crystals appear to have overgrown irregular and corroded Py_{1a} grains (Fig. 5b). Some of the Py_{1b} grains are truncated by grain boundaries (Fig. 5b) consistent with the partial dissolution of pyrite (Cook et al. 2009). After Py_1 formation, oscillatory-zoned Py_{2a}, accompanied by a few quartz, precipitated during Stage II (Figs. 5c-f). Oscillatory zoning, a common feature in auriferous pyrite, has been documented in many gold deposits (e.g., Peterson and Mavrogenes 2014). Periodic and repetitive changes in pressure (P), temperature (T), and bulk fluid composition have been invoked to explain this zoning (Velásquez et al. 2014). Episodic fluctuations in fluid compositions from multiple hydrothermal events generally lead to several stages of pyrite precipitation with distinct sulfur isotope compositions, irregular boundaries, and corrosion textures between alternating bands (Barker et al. 2009). None of these features has been observed in the Py_{2a}, ruling out a multi-stage pyrite crystallization model. Instead, episodic changes of physico-chemical parameters (e.g., P-T-pH) during the boiling of the ore fluids are invoked.

Previous studies suggested that zoning in pyrite reflected rapid variations in the As content of ore fluids through time (Deditius et al. 2014; Velásquez et al. 2014). Ballantyne and Moore (1988) proposed that the As concentration of hydrothermal fluids is inversely proportional to the partial pressure of H_2S in geothermal systems and their fossil analogs, the epithermal deposits. The Qiucun

348 hydrothermal system was relatively shallow, and repeated boiling is manifested in hydrothermal
349 breccias and hydraulic fracturing, and in the features of auriferous veins (colloform banded and
350 vuggy quartz veins and bladed calcite crystals) and fluid inclusions (Ni et al. 2018). In such a system,
351 rapid fluctuations in pressure, from hydrostatic to lithostatic, could have been caused by fracturing
352 and resealing of fluid conduits. These variations, and the accompanying boiling, could also
353 contribute to the rapid changes in pH and variations and the activity of sulfur, thus in the solubility of
354 As in the ore fluid (e.g., Kouzmanov and Pokrovski 2012). Moreover, the removal of volatiles (H_2S
355 and CO_2) into vapor tends to increase the pH of the solution, which decreases the solubility of
356 sulfides. Therefore, the cyclicity of pyrite banding reflects repeated and sudden variations in fluid
357 pressure and transient fluid flow regimes.

358 ***Gold in Py_{1b} and Py_{2a}***: Rims of Py_1 and the oscillatory-zoned Py_{2a} all contain invisible gold, as is
359 the case for Py_1 cores. However, the As-rich bands in Py_{1b} and oscillatory-zoned Py_{2a} have about one
360 to two magnitudes more Au than the $Py_{1a,}$ whereas the As-poor bands contain less Au than Py_{1a}. This
361 relationship is also well-revealed by LA-ICP-MS images, an apparent Au enrichment coinciding
362 with As-rich bands in these pyrite generations (Figs. 11-12). There is also a positive correlation
363 between As and Au (Fig. 9a), which is consistent with the preferential precipitation of gold in
364 As-rich layers (e.g., Deditius et al. 2014). It is generally accepted that As-rich sulfides play an
365 important role in scavenging gold (Simon et al. 1999). Fluid boiling at moderate temperatures as
366 documented for Qiucun (<250°C; Ni et al. 2018) is a very efficient way of precipitating most
367 minerals from the liquid phase (Heinrich 2007). Arsenic, Au, Fe, and most other metallic elements
368 exhibit vapor-liquid partitioning coefficients mainly in favor of the liquid phase at temperatures
369 below 300°C (Kouzmanoy and Pokrovski 2012), and thus precipitate from the liquid phase if the
370 extent of phase separation is high enough to remove a sufficient part of H_2O into the vapor and thus
371 oversaturate the liquid with arsenian pyrite and native gold.

372 **Secondary gold enrichment**

373 **Formation of gold- and trace element-rich Py_{2b}**

374 Coupled dissolution-reprecipitation (CDR) reactions have proven significant for the remobilization
375 and upgrading of sulfide-hosted gold ores in various types of gold deposits (Sung et al. 2009; Hasite
376 et al. 2020). Later hydrothermal fluids dissolve parts of the parent mineral in the CDR processes and
377 precipitate a compositionally different daughter phase at nanometer scale. The resulting product is
378 characterized by high porosity and preserving the external shape and crystallographic orientation of
379 the replaced grain (Putnis 2009). Textural observations suggest that porous Py_{2b} occurs preferentially
380 along microfractures and grain margins of Py_{2a} (Figs. 5g-i). The reaction front is sharp and
381 curvilinear (Fig. 5h), which is strong evidence of CDR reactions (Putnis 2009). These textures
382 suggest a fluid dissolved earlier Py_{2a}, which was then re-precipitated as Py_{2b}. Preservation of the
383 external morphology of parent Py_{2a} (Figs. 5g-i) indicates some degree of a spatial and temporal
384 coupling between the dissolution and re-precipitation (Wu et al. 2019).

385 The *in situ* LA-ICP-MS analyses in the spot- and mapping-modes highlight systematic trace
386 element variations between different pyrite generations in Stage II veins (Figs. 8-9, 12). During the
387 replacement of Py_{2a} by porous Py_{2b}, elements concentrated in Py_{2b} relative to Py_{2a} (Au, As, Ag, Sb,
388 Pb, Tl, and Cu) might be sourced from infiltrating fluids or from sulfides hosted in sub-micron
389 inclusions (e.g., electrum, galena, chalcopyrite, and arsenopyrite) formed during remobilization from
390 earlier pyrite generations. The peaks of ^{65}Cu, ^{121}Sb, ^{197}Ag, and ^{208}Pb in LA-ICP-MS laser profiles
391 (Gregory et al. 2016; Supplementary Appendix Fig. A1F) support the existence of such
392 sub-microscopic sulfide inclusions in Py_{2b}. The presence of Au, Cu, Pb, Ag, and Sb-bearing minerals
393 in later alteration pyrite-arsenopyrite assemblages formed through trace element remobilization and
394 secondary enrichment during CDR reactions has also been documented in many other gold deposits
395 (e.g., Sung et al. 2009; Hastie et al. 2020).

396 **Visible gold in pyrite ores**

Cycles of hydrothermal infiltration during ore deposit formation can alter pre-existing ore minerals and remobilize gold, among other chemical constituents (e.g., Morey et al. 2008; Cook et al. 2013). For example, visible gold concentrated around the grain boundaries and fractures of pyrite and arsenopyrite is very common in orogenic gold deposits worldwide. It has been interpreted to form via the hydrothermal alteration of pre-existing auriferous sulfides during an increase in temperature and sulfur fugacity during prograde metamorphism (Morey et al. 2008; Lawley et al. 2017). For example, at Sunrise Dam, Australia, textural evidence exists that is consistent with the replacement of arsenian pyrite, whereby remobilized gold was deposited as native gold inclusions oriented parallel to crystal faces or in fractures, inferring the partial replacement of parent arsenian pyrite via fluid-mediated CDR reactions (Sung et al. 2009). Furthermore, oscillatory- and sector-zoned pyrite from Jerome and Kenty deposits in Canada records textures, such as porosity development coincident with the presence of native gold and accessory sulfide phases, which are suggestive of CDR reactions that liberated gold and associated elements from earlier auriferous pyrite (Hastie et al. 2020).

At Qiucun, visible electrum grains occur as inclusions within all pyrite generations, as solitary grains or veins in fractures at grain boundaries in pyrite (Fig. 6). The visible gold-bearing pyrite grains (Fig. 6) are pervasively fractured, have irregular grain boundaries, and BSE images reveal that these pyrite grains have intra-granular compositional zones that are possibly related to a dynamic alteration history. Parallel to the fractures and boundaries, or intra-grain narrow composite rims within the auriferous pyrite are characterized by a higher than average atomic mass (Fig. 6). These rims vary in their dimensions but are, in general, up to 300 μm in thickness from grain boundaries and fracture margins. As shown in Figures 6a-c, the rims are porous and define zones in which selective chemical modification of the preexisting pyrite parallel to fracture-grain boundaries has taken place. This grain boundary-fracture association indicates an external (i.e., post-formation) influence. Due to the lack of other mineral phases containing As and S, the infiltration of a later hydrothermal fluid is considered responsible. This fluid would have infiltrated along grain

boundaries, possibly promoting fracturing and facilitating the reaction process. The resulting pyrite rims are thus thought to be alteration rims.

The precipitation of invisible gold, followed by the later formation of visible gold, is schematically illustrated in Figure 14. Given that primary pyrite grains are characterized by relatively uniform invisible gold within single generations and that alteration rims (which replaced primary growth phases) are depleted in invisible gold, it is suggested that early refractory gold exsolved and was then remobilized locally to form at least part of the later visible gold. The formation of visible gold by hydrothermal alteration of refractory gold-bearing pyrite may provide new insights into the formation of high-grade gold ores in epithermal deposits, although the direct introduction of gold by later auriferous fluids cannot be ruled out. It is suggested here that fluids reacted with fractured auriferous pyrite, causing CDR reactions, during repeated, episodic brittle deformation events. Invisible gold, together with some of the low-melting-point elements (e.g., Cu, Pb, and Sb) were dissolved and re-precipitated as visible gold, galena, and chalcopyrite, within the same pyrite grain as inclusions, as well as in fractures within pyrite (Fig. 14).

Sulfur isotopic fingerprint of ore-forming processes

Early pyrite generations (Py_{1-2a}) from the auriferous veins at Qiucun yielded a narrow range of $\delta^{34}S_{py}$ of -3.6 to 4.6 ‰ with an average of 0.3 ‰, independent of pyrite generation (Figs. 13a-b). The temperature of the ore fluid at Qiucun is thought to be within the range of 180° to 250°C based on microthermometry of fluid inclusions in the quartz from vein-type ores (Ni et al. 2018). Assuming a temperature of 250°C, the corresponding range and mean $\delta^{34}S_{H2S}$ values are -5.1 to 3.1 ‰ and -1.2 ‰, respectively. The $\delta^{34}S$ values reported here are also very close to those in nearby magmatic-hydrothermal deposits (e.g., the Ancun, Xiaban, Dongyang Au deposits), which are generally in the range of -4 to 2 ‰ (Li et al. 2018a, b). This demonstrates that most of the gold deposits in the Dehua goldfield had a similar magmatic sulfur source. The Co and Ni contents reported here for pyrite from the Qiucun deposit are similar to those in epithermal Au-Ag

hydrothermal systems (Fig. 9i). The dominant range of Co/Ni ratios between 0.5 and 10 is consistent with pyrite of a magmatic-hydrothermal origin (Reich et al. 2016).

There is a very slight variation of $\delta^{34}S$ values (-1.5 to 1.3‰) in a single oscillatory-zoned Py_{2a} grain (Fig. 5e), illustrating a systematic decoupling from the trace element distribution, which was controlled by pressure fluctuations and repeated localized fluid boiling as discussed earlier. Previous studies have suggested that $\delta^{34}S$ ratios of sulfide minerals are strongly influenced by oxygen fugacity (fO_2), pH, temperature, and the composition of the parental fluid, but the pressure effect is limited (e.g., Ohmoto 1972; Seal 2006; Li et al. 2018). Therefore, the localized pressure fluctuations and subsequent fluid boiling were not enough to generate sulfur isotope fractionation in oscillatory-zoned pyrite grains. However, the *in situ* $\delta^{34}S$ ratios for the Py_2 rims (Py_{2b}: -15.2 to -2.3‰) are distinctly lighter than the cores in all the analyzed samples: the average Py_{2b} is 8.0‰ lighter than the Py_{2a}. The negative $\delta^{34}S$ values in Py_{2b} either reflect a sulfur source contribution of negative $\delta^{34}S$ from the sedimentary host rocks or isotopic fractionation due to change of temperature and oxygen fugacity along with the evolution of the ore fluids. Because no significant amounts of negative $\delta^{34}S$ sedimentary rocks has been found in any lithological unit in the Dehua gold field, we consider changes in the physicochemical conditions (e.g., temperature, pH, and fO_2; Ohmoto 1972; Ma et al. 2021b) during pyrite precipitation was a likely explanation for the negative $\delta^{34}S$ values of Py_{2b}. During main-stage pyrite mineralization, a shift from sericite to illite alteration (Ni et al. 2018) reflects cooling of the ore fluid. Pyrite is estimated to be 1.5 ‰ heavier than H_2S in the hydrothermal fluid at 250°C, whereas the pyrite-H_2S fractionation is about 1.9 ‰ at 180°C (Ohmoto and Rye 1979). Cooling of the ore fluid by 70°C could cause a ~0.4 ‰ increase in pyrite $\delta^{34}S$, and therefore, temperature decrease alone cannot explain the observed decrease in $\delta^{34}S$ ratios in Py_{2b}. The pH of Stage II vein formation had a narrow range of 5.6 to 6.7, based on observation that the mineralization was associated with sericite-illite alteration and the occurrence as a gangue mineral (Ni et al., 2018). Thus, the pH value should not significantly affect the sulfur isotopic composition either.

More significant changes in $\delta^{34}S$ ratios can result from changes in the proportions of oxidized and reduced sulfur species in the ore fluid (e.g., Ohmoto 1972). Fluid oxidation has been commonly suggested to cause negative $\delta^{34}S$ ratios in sulfides and rapid gold deposition in hydrothermal ore deposits (LaFlamme et al. 2018). Fractionation of heavy ^{34}S into the oxidized sulfur species would cause ^{34}S-depleted H_2S in the residual hydrothermal fluid. Consequently, pyrite deposited from the fluid after oxidation would be characterized by much lower $\delta^{34}S$ ratios relative to pyrite precipitated before oxidation (Ohmoto 1972). At the shallow crustal levels recorded at Qiucun (~ 260 m; Ni et al. 2018), it is suggested that, during the later mineralization stage, cooler and oxidized meteoric water was increasingly involved in the precipitation of the last generation of pyrite (Py_{2b}), leading to the further oxidation of the mineralizing fluids and consequently lowering of $\delta^{34}S$ (Fig. 13).

IMPLICATIONS

In this contribution, two main types of Au mineralization are recognized at Qiucun, with distinct mechanisms: (i) Primary precipitation of invisible gold within unaltered pyrite domains (Py_{1a}, Py_{1b}, and Py_{2a}). We relate the textural and geochemical features of these pyrites to their depositional mechanisms: Py_{1a} with low concentrations of As and Au is contemporary with the early hydrothermal alteration of biotite in the host rock and commonly occurs as cores of pyrite. The Py_{1b} and Py_{2a} with characteristics oscillatory zoning of As and Au formed at Stages I-II. This oscillatory zoning is interpreted to have resulted from pressure fluctuation and repeated fluid boiling around the pyrite crystals. Invisible gold is present throughout these pyrite crystals but is more abundant in the As-rich bands; (ii) Secondary enrichment of visible and invisible gold (hosted by Py_{2b}) associated with later-stage alteration events produced chemically modified alteration rims on the auriferous pyrite. Results of LA-ICP-MS analyses suggest that Au and other trace elements (As, Ag, Sb, Pb, Tl, and Cu) that had been initially incorporated in Py_{2a} were partly expelled and remobilized during replacement of porous and trace element (including Au)-rich Py_{2b}. The very low $\delta^{34}S$ values recorded

497 by Py_{2b} suggest the partial dissolution of Py_{2a} and re-precipitation of Py_{2b} under increasing oxygen
498 fugacity. An additional consequence of the reactivation process is the fracturing of the previously
499 formed auriferous pyrite that continued through later brittle deformation events, which led to more
500 fracturing of pyrite. This newly created porosity of pyrite facilitated further fluid flow along the
501 margins of fractures and grain boundaries within pyrite, including hydrothermal alteration of pyrite
502 and dissolution of invisible gold, which re-precipitated as small inclusions and in fractures as larger
503 veins. This study highlights that the textural, geochemical, and sulfur isotopic compositions of pyrite
504 can provide critical information not only for the physicochemical conditions of the initial gold
505 deposition but also for the secondary invisible and visible gold enrichment processes in Au deposits.
506
507
508 ## ACKNOWLEGEMENTS AND FUNDING

509 This study was supported by the National Natural Science Foundation of China (grant no. 41973044),
510 the MOST Special Fund from the State Key Laboratory of Geological Processes and Mineral
511 Resources, China University of Geosciences (grant no. MSFGPMR03-2), and the Fundamental
512 Research Funds for National Universities, China University of Geosciences (Wuhan) (grant no
513 2201610076). Our thanks extend to the Qiucun Mining Ltd. and the Fujian Institute of Geological
514 Survey and Research for providing access to samples and information about the deposit. Kui-Dong
515 Zhao, Wei Chen, Fang-Yue Wang, Jian-Feng Gao, Liang Li, and Pei-Jun Lin are also thanked for
516 their help with lab work. We certify that we have no potential conflicts of interest including relevant
517 financial interests. Constructive reviews by Dr. Daniel Gregory and Dr. Xing-Hui Li, and editorial
518 comments and suggestions by editor Dr. Matthew Steele-MacInnis have been very helpful in our
519 revision and are gratefully acknowledged.
520
521

REFERENCES CITED

Ballantyne, J.M., and Moore, J.N. (1988) Arsenic geochemistry in geothermal systems. Geochimica et Cosmochimica Acta, 52, 475-483.

Barker, S.L.L., Hickey, K.A., Cline, J.S., Dipple, G.M., Kilburn, M.R., Vaughan, J.R., and Longo, A.A. (2009) Unlocking invisible gold: use of nanoSIMS to evaluate gold, trace elements, and sulfur isotopes in pyrite from Carlin-type gold deposits. Economic Geology, 104, 879-904.

Cook, N.J., Ciobanu, C.L., and Mao, J.W. (2009) Textural control on gold distribution in As-free pyrite from the Dongping, Huangtuliang, and Hougou gold deposits, North China craton (Hebei Province, China). Chemical Geology, 264, 101-121.

Deditius, A., Utsunomiya, S., Reich, M., Kesler, S., Ewing, R., Hough, R., and Walshe, J. (2011) Trace metal nanoparticles in pyrite. Ore Geology Reviews, 42, 32-46.

Deditius, A.P., Reich, M., Kesler, S.E., Utsunomiya, S., Chryssoulis, S.L., Walshe, J.L., Hough, R., and Ewing, R.C. (2014) The coupled geochemistry of Au and As in pyrite from hydrothermal ore deposits. Geochimica et Cosmochimica Acta 140, 644-670.

Fan, K. (2015) Geological characteristics and prospecting direction of Qiucun gold mine in Dehua county, Fujian province. Modern Mining, 560, 84-86 (in Chinese with English abstract).

Franchini, M., McFarlane, C., Maydagán, L., Reich, M., Lentz, D.R., Meinert, L., and Bouhier, V. (2015) Trace metals in pyrite and marcasite from the Agua Rica prophyry-high sulfidation epithermal deposit, Catamarca, Argentina: Textural features and metal zoning at the porphyry to epithermal transition. Ore Geology Reviews, 66, 366-387.

Gao, J-.F, Jackson, S.E, Dube, B., and De Souza, S. (2015) Genesis of the Canadian Malartic, Côté Gold, and Musselwhite gold deposits: Insights from LA-ICP-MS element mapping of pyrite. In: Targeted Geoscience Initiative 4: Contributions to the Understanding of Precambrian Lode Gold Deposits and Implications for Exploration (eds) B. Dubé and P. Mercier-Langevin; Geological Survey of Canada: Open File 7852.

Gregory, D.D., Large, R.R., Bath, A.B., Steadman, J.F., Wu, S., Danyushevsky, L., Bull, S.W., Holden, P. and Ireland, T.R. (2016) Trace element content of pyrite from the Kapai Slate, St. Ives Gold District, Western Australia. Economic Geology, 111, 1297-1230.

549 Gregory, D.D., Large, R.R., Halpin, J.A., Baturina, E.L., Lyons, T.W., Wu, S., Danyushevsky, L., Sack, P.J.,
550 Chappaz, A. and Maslennikov, V.V. (2015) Trace element content of sedimentary pyrite in black shales.
551 Economic Geology, 110, 1389-1410.
552 Gregory, D.D., Cracknell, M.J., Large, R.R., McGoldrick, P., Kuhn, S., Maslennikov, V.V., Baker, M.J., Fox, N.,
553 Belousov, I., Figueroa, M.C., Steadman, J.A., Fabris, A.J., and Lyons, T.W. (2019) Distinguishing ore deposit
554 type and barren sedimentary pyrite using laser ablation-inductively coupled plasma-mass spectrometry trace
555 element data and statistical analysis of large data sets. Economic Geology, 114, 771-786.
556 Gopon, P., Douglas, J.A., Auger, M.A., Hansen, L., Wade, J., Cline, J.S., Robb, L.J., and Moody, M.P. (2019) A
557 nanoscale investigation of Carlin-type gold deposits: An atom-scale elemental and isotopic prospective.
558 Economic Geology, 114, 1123-1133.
559 Gourcerol, B., Kontak, D.J., Thurston, P.C., and Petrus, J.A. (2018) Results of LA-ICP-MS sulfide mapping from
560 Algoma-type BIF gold systems with implications for the nature of mineralizing fluids, metal sources, and depo
561 sit models. Mineralium Deposita, 53, 871-894.
562 Haroldson, E.L., Beard, B.L., Satkoski, A.M., Brown, P.E. and Johnson, C. (2018) Gold remobilization associated
563 with Mississippi Vallwy-type fluids: A Pb isotope perspective. GSA Bulletin 130, 1583-1595.
564 Hastie, E.C.G., Kontak, D.J., and Lafrance, B. (2020) Gold remobilization: Insights from gold deposits in the
565 Archean Swayze Greenstone Belt, Abitibi Subprovince, Canada. Economic Geology, 115, 241-277.
566 Heinrich, C.A. (2007) Fluid-fluid interactions in magmatic-hydrothermal ore formation. Review in Mineralogy and
567 Geochemistry, 65, 363-387.
568 Huang, B., Ni, P., Xiang, H.L., Wang, G.G., Yang, Y.L., Pan, J.Y., Li, S.N., Bao, T. (2017) The Geological
569 characteristics and ore genesis of the Qiucun gold deposit, Fujian Province. Bulletin of Mineralogy, Petrology
570 and Geochemistry, 36, 650-658 (in Chinese with English abstract).
571 Jiang, Q.Y. (2015) Geological characteristics and prospecting significance of Dongyang gold deposit in Dehua
572 County, Fujian Province. Geol. Fujian 34, 27-32 (in Chinese with English abstract).
573 Jochum, K.P., Willbold,M., Raczek, I., Stoll, B. and Herwig, K. (2005) Chemical characterisation of the USGS
574 reference glasses GSA-1G, GSC-1G, GSD-1G, BCR-2G, BHVO-2G and BIR-1G using EPMA, ID-TIMS,
575 ID-ICP-MS and LA-ICP-MS. Geostandards and Geoanalytical Research, 29: 285-302.
576 Kerr, M.J., Hanley, J.J., Kontak, D.J., Morrison, G.G., Petrus, J., Fayek, M., and Zajacz, Z. (2018) Evidence of upg
577 rading of gold tenor in an orogenic quartz-carbonate vein system by late magmatic-hydrothermal fluids at the

578 Madrid Deposit, Hope Bay Greenstone Belt, Nunavut, Canada. Geochimica et Cosmochimica Acta, 241, 180-
579 218.
580 Kouzmanov, K. and Pokrovski, G.S. (2012) Hydrothermal controls on metal distribution in Cu (-Au-Mo) porphyry
581 systems. SEG Special Publication 16, 573-618.
582 LaFlamme, C., Sugiono, D., Thebaud, N., Caruso, S., Fiorentini, M., Selvaraja, V., Jeon, H., Voute, F. and Martin,
583 L. (2018) Multiple sulfur isotopes monitor fluid evolution in an orogenic gold deposit. Geochimica et
584 Cosmochimica Acta, 222, 436-446.
585 Large, R.R., Bull, S.W. and Maslennikov, V.V. (2011) A carbonaceous sedimentary source-rock model for
586 Carlin-type and orogenic gold deposits. Economic Geology, 106: 331-358.
587 Large, R.R., Danyushevsky, L., Hollit, C., Maslennikov, V., Meffre, S., Gilbert, S., Bull, S., Scott, R., Emsbo, P.,
588 Thomas, H., Singh, B. and Foster, J. (2009) Gold and trace element zonation in pyrite using a laser imaging
589 technique: Implications for the timing of gold in orogenic and Carlin-style sediment-hosted deposits.
590 Economic Geology, 104, 635-668.
591 Lawley, C.J.M., Jackson, S., Yang, Z., Davis, W., and Eglington, B. (2017) Tracing the transition of gold from
592 source to sponge to sink. Economic Geology, 112, 169-183.
593 Li, S-.N., Ni, P., Bao, T., Li, C-.Z., Xiang, H-.L., Wang, G-.G., Huang, B., Chi, Z., Dai, B-.Z., and Ding, J-.Y.
594 (2018a) Geology, fluid inclusion, and stable isotope systematics to the Dongyang epithermal gold deposit,
595 Fujian Province, southeast China: Implications for ore genesis and mineral exploration. Journal of
596 Geochemical Exploration, 195, 16-30.
597 Li, S-.N., Ni, P., Bao T., Xiang, H-.L., Chi, Z., Wang, G-.G., Huang, B., Ding, J-.Y. and Dai, B-.Z. (2018b)
598 Genesis of the Ancun epithermal gold deposit, southeast China: Evidence from fluid inclusion and stable
599 isotope data. Journal of Geochemical Exploration, 195, 157-177.
600 Li, S-.N., Ni, P., Wang, G-.G., Bao, T., Huang, B. and Dai, B-.Z. (2020) The Jurassic volcanic-intrusive complex in
601 the Dehua gold orefield, coastal region of SE China: Implications for the tectonic setting and epithermal
602 mineralization. Journal of Asian Earth Sciences 197, 104390.
603 Li, X-.H., Fan, H-.R., Yang, K-.F., Hollings, P., Liu, X., Hu, F.F. and Cai Y-.C. (2018) Pyrite textures and
604 compositions from the Zhuangzi Au deposit, southeastern North China Craton: implication for ore-forming
605 processes. Contributions to Mineralogy and Petrology, 173: 73.

606 Liu, Y., Hu, Z., Gao, S., Xu, J., Gao, C., and Chen, H. (2008) In situ analysis of major and trace elements of
607 anhydrous minerals by LA-ICP-MS without applying an internal standard. Chemical Geology, 257, 34-43.
608 Liu, Q-.S. (2018) Geological characters and ore-forming material sources of the Qiucun gold deposit. World
609 Nonferrous Metal, 11, 85-86 (in Chinese with English abstract).
610 Ma, Y., Jiang, S-.Y., Frimmel, H.E., Xiong, S-.F., Zhu, L-.Y. and Chen, R-.S. (2021a) Early Paleozoic Orogenic
611 Gold Deposit in the Cathaysia Block, China: A first example from the Shuangqishan Deposit. Gondwana
612 Research, 91, 231-253.
613 Ma, Y., Jiang, S-.Y., Frimmel, H.E., Zhu, L-.Y., Xiong, S-.F., Chen, R-.S. and Li, X-.X. (2021b) Genesis of the
614 Hebaoshan gold deposit in Fujian Province of Southeast China: constraints from a combined fluid inclusion,
615 H-O-C-S-Pb-He-Ar isotope and geochronological study. https://doi.org/10.1007/s00126-021-01046-3.
616 Migdisov, A.A., Zezin, D. and Williams-Jones, A.E. (2011) An experimental study of cobalt (II) complexation in
617 Cl^- and H_2S-bearing hydrothermal solutions. Geochimica et Cosmochimica Acta 75, 4065-4079.
618 Morey, A.A., Tomkins, A.G., Bierlein, F.P, Weinberg, R.F. and Davidson, G.J. (2008) Bimodal distribution of gold
619 in pyrite and arsenopyrite: Examples from the Archean Boorara and Bardoc shear systems, Yilgarn craton,
620 Western Australia. Economic Geology, 103, 599-614.
621 Ni, P., Pan, J.Y., Huang, B., Wang, G.G., Xiang, H.L., Yang, Y.L., Li, S.N. and Bao, T. (2018) Geology,
622 ore-forming fluid and genesis of the Qiucun gold deposit: Implication for mineral exploration at Dehua
623 prospecting region, SE China. Journal of Geochemical Exploration, 195, 3-15.
624 Ohmoto, H. (1972) Systematics of sulfur and carbon isotopes in hydrothermal ore deposits. Economic Geology, 67,
625 551-578.
626 Ohmoto, H. and Rye, R.O. (1979) Isotopes of sulfur and carbon. In: Barnes HL (ed) Geochemistry of hydrothermal
627 ore deposits. Wiley, New York, 509-567.
628 Peterson, E. and Mavrogenes, J. (2014) Linking high-grade gold mineralization to earthquake-induced fault-valve
629 processes in the Porgera gold deposit, Papua New Guinea. Geology, 42, 383-386.
630 Putnis, A. (2009) Mineral replacement reactions. Reviews in Mineralogy and Geochemistry, 70, 87-124.
631 Reich, M., Simon, A., Deditius, A., Barra, F., Chryssoulis, S., Lagas, G., Tardani, D., Knipping, J., Bilenker, L.,
632 Sánchez-Alfaro, P., Roberts, M.P. and Munizaga, R. (2016) Trace element signature of pyrite from the Los
633 Colorados iron oxide-apatite (IOA) deposit, Chile: A missing link between Andean IOA and iron oxide
634 copper-gold systems? Economic Geology, 11, 743-761.

635 Reich, M., Kesler, S.E., Utsunomiya, S., Palenik, C.S., Chryssoulis, S.L. and Ewing, R.C. (2005) Solubility of gold
636 in arsenian pyrite. Geochimica et Cosmochimica Acta 69, 2781-2796.
637 Shu, L., Wang, B., Cawood, P.A., Santosh, M. and Xu, Z. (2015) Early Paleozoic and Early Mesozoic intraplate
638 tectonic and magmatic events in the Cathaysia Block, South China. Tectonics 34, 1600-1621.
639 Simon, G., Kesler, S.E. and Chryssoulis, S. (1999) Geochemistry and textures of gold-bearing arsenian pyrite,
640 Twin Creeks, Nevada: Implications for deposition of gold in Carlin-type deposits. Economic Geology, 94,
641 405-421.
642 Sung, Y.-H., Brugger, J., Ciobanu, C., Pring, A., Skinner, W. and Nugus, M. (2009) Invisible gold in arsenian
643 pyrite and arsenopyrite from a multistage Archaean gold deposit: Sunrise dam, Eastern Goldfields province,
644 Western Australia. Mineralium Deposita, 44, 765-791.
645 Sykora, S., Cook, D.R., Meffre, S., Stephanov, A.S., Gardner, K., Scott, R., Selley, D. and Harris, A.C. (2018)
646 Evolution of pyrite trace element compositions from porphyry-style and epithermal conditions at the Lihir
647 gold deposit: implications for ore genesis and mineral processing. Economic Geology, 113, 193-208.
648 Velásquez, G., Béziat, D., Salvi, S., Sienenaller, L., Borisova, A.Y., Pokrovski, G.S. and Parseval, P.D. (2014)
649 Formation and deformation of pyrite and implications for gold mineralization in the El Callao District,
650 Venezuela. Economic Geology, 109, 457-486.
651 Wang, F.Y., Ge, C., Ning, S.Y., Nie, L.Q., Zhong, G.X. and Nole, C.W. (2017) A new approach to LA-ICP-MS
652 mapping and application in geology. Acta Petrologica Sinica 33, 3422-3436 (in Chinese with English
653 abstract).
654 Wang, J. and Li, Z.X. (2003) History of Neoproterozoic rift basins in South China: implications for Rodinia
655 break-up. Precambrian Research, 122, 141-158.
656 White, N.C., Zhang, D., Hong, H., Liu, L., Sun, W. and Zhang, M. (2019) Epithermal gold deposits of China: An
657 overview. SEG Special Publication 22, 235-262.
658 Williams-Jones, A.E., Bowell, R.J. and Migdisov, A.A. (2009) Gold in solution. Elements 5, 281-287.
659 Wilson, S.A., Ridley, W.I. and Koenig, A.E. (2002) Development of sulfide calibration standards for the laser
660 ablation inductively coupled plasma mass spectrometry technique. Journal of Analytical Atomic Spectrometry,
661 17, 406-409.

Wohlgemuth-Ueberwasser, C.C. and Jochum, K.P. (2015) Capability of fs-LA-ICP-MS for sulfide analysis in comparison to ns-LA-ICP-MS: reduction oflaser induced matrix effects? Journal of Analytical Atomic Spectrometry, 30: 2469-2480.

Wu, F.Y., Lin, J.Q., Wild, S.A., Zhang, X.O. and Yang, J.H. (2005) Nature and significance of the Early Cretaceous giant igneous event in eastern China. Earth Planetary Science Letters, 223, 103-119.

Wu, Y-.F., Evans, K., Li, J-.W., Fougerouse, D., Large, R.R. and Guagliardo, P. (2019) Metal remobilization and ore-fluid perturbation during episodic replacement of auriferous pyrite from an epizonal orogenic gold deposit. Geochimica et Cosmochimica Acta 245, 98-117.

Zhang, H., Cai, Y., Zhang, Y., Ni, P., Li, S., Ding, J., Pan, Y. and Bao, T. (2018) Mineralogical characteristics of silver minerals from the Dongyang Gold deposit, China: Implications for the evolution of epithermal metallogenesis. Journal of Geochemical Exploration, 195, 143-156.

Zhai, D., Williams-Jones, A.E., Liu, J., Selby, D., Voudouris, P.C., Tombros, S., Li, K., Li P. and Sun, H. (2020) The genesis of the giant Shuangjianzishan epithermal Ag-Pb-Zn deposit, Inner Mongolia, Northeastern China. Economic Geology, 115, 101-128.

Zhong, J., Pirajno, F. and Chen, Y.J. (2017) Epithermal deposits in South China: Geology, geochemistry, geochronology, and tectonic setting. Gondwana Research, 42, 193-219.

Zhou, X.M., Sun, T., Shen, W.Z., Shu, L.S. and Niu, Y.L. (2006) Petrogenesis of Mesozoic granitoids and volcanic rocks in South China: A response to tectonic evolution. Episodes 29, 26-33.

Zhu, Z.Y., Cook, N.J., Yang, T., Ciobanu, C.L., Zhao, K.D. and Jiang, S.Y. (2016) Mapping of S isotopes and trace elements in sulfides by LA-(MC)-ICP-MS: potential analytical problems, improvements and implications. Minerals 6, 110.

Figure Captions

Fig. 1. (a) Simplified map of the tectonic units of eastern China (Wu et al. 2005); (b) Geologic map of the Coastal Volcanic Belt in southeastern China showing major faults, Late Mesozoic igneous rocks, and epithermal gold deposits (modified from Zhong et al. 2017).

690 **Fig. 2.** (a) Regional geologic map of the Dehua area showing the distribution of the gold deposits
691 (modified from Jiang 2015); Geologic map (b) and representative cross-section (c) of the Qiucun
692 deposit, showing distribution and morphology of the gold orebodies (after Huang et al. 2017).
693
694 **Fig. 3.** Photographs illustrating textures of gold ores of the Qiucun gold deposit. (a) Quartz veins
695 crosscutting the disseminated pyrite ores. (b) Smoky-gray quartz-chalcedony-pyrite vein of Stage I
696 within the volcanic rocks of the Nanyuan Formation. (c) Stage I veins showing the
697 quartz-chalcedony-pyrite-cemented breccias of wall rocks. (d) Stage III quartz-sulfides veins
698 crosscutting the sandstone of the Changlin Formation. (e) Quartz-sulfides cementing and cutting wall
699 rocks breccias. (f) Stage III quartz-calcite vein with pyrite as anhedral aggregates near the vein
700 margin. ***Abbreviations:*** Cal-calcite, Py-pyrite, Qz-quartz.
701
702 **Fig. 4.** Paragenetic sequence of Qiucun gold mineralization interpreted from textures and pyrite
703 geochemistry; Line thickness indicates approximate relative mineral abundance. ***Abbreviation:***
704 Py-pyrite.
705
706 **Fig. 5.** Backscattered-electron (BSE) images showing textural features and relationships of different
707 generations of pyrite at Qiucun, also shown are the spots of in-situ $\delta^{34}S_{V\text{-}CDT}$ (‰) isotope
708 composition of pyrite: : (a) Py_{1a} with abundant silicate inclusions; (b) Py_{1b} overgrowths on Py_{1a}; (c)
709 Early generation of sulfides, including Py_{1a} and Py_{1b}, are overgrown by oscillatory-zoned Py_{2a} and
710 the outer rim of As-rich Py_{2b} bands. Note that electrum in fracture of pyrite accompanied by quartz;
711 (d) Porous and inclusion-rich Py_1 is overgrown by oscillatory-zoned Py_{2a}, note that electrum filling
712 the microfracture of the Py_{2a}; (e) Py_{2a} with characteristic zoning; (f) Cluster of euhedral fine-grained
713 Py_{2a} grains; (g-i) Inclusion-free, zoned Py_{2a} is surrounded by porous and As-rich Py_{2b}. Note that
714 sharp and curvilinear interfaces among them. ***Abbreviations:*** Elc-electrum, Py-pyrite.

715

716 **Fig. 6.** Collection of backscattered-electron images defining the characteristics of alteration zones
717 within visible gold-bearing pyrite in the Qiucun gold deposit. (a) A pyrite grain from the Stage I vein
718 showing the association later-stage between alteration rims and visible gold. (b) Anhedral Py_{2a} grains
719 showing advanced stages of post-formation alteration rim around the grain boundary. Visible
720 electrum grains occur as inclusions in alteration rims, in fractures within them, or along grain
721 boundaries. (c) Pyrite from the Stage II veins, showing intergrain rims and the association between
722 alteration rims and visible gold. (d) Electrum filling the fractures of the altered Py_{2a} grains.
723 ***Abbreviations:*** Elc-electrum, Gn-galena, Py-pyrite, Qz-quartz

724

725 **Fig. 7.** (a) Ternary diagram showing the As-Fe-S composition of pyrite; Only EPMA data were
726 considered. Five different trends show substitution of (i) As for S (As^{-1} pyrite); (ii) As^{0}
727 nano-inclusions; (iii) As^{2+} for Fe (As^{2+} pyrite); (iv) As^{3+} for Fe (As^{3+} pyrite); and divalent metals
728 (Me^{2+}) substituting isovalently for Fe (after Deditius et al. 2008, 2014). (b) A plot of As vs. S
729 concentrations for the pyrite, showing a good linear inverse correlation between these elements.

730

731 **Fig. 8.** Trace element distribution diagram showing the variation in the Co, Ni, Cu, Zn, As, Ag, Sb,
732 Au, Pb, and Bi concentrations (in ppm) for all pyrite generations; Concentrations are in logarithmic
733 scale.

734

735 **Fig. 9.** Elemental concentration scatterplots for different generations of pyrite from the Qiucun
736 deposit. (a) Au vs. As: almost all the pyrite generations show a positive relationship with Au-As. All
737 the data spots are below the gold solubility line in pyrite (Reich et al. 2005); (b) Au vs. Ag; (c) Au vs.
738 Cu; (d) Ag vs. Sb; (e) Ag vs. Cu; (f) Ag vs. Pb; (g) Tl vs. Sb; (h) Cu vs. Pb; (i) Co vs. Ni.

739

740 **Fig. 10.** LA-ICP-MS element maps with logarithmic color scales (in ppm) showing contents and
741 distribution patterns of trace elements of a representative pyrite grain from Stage I. Numbers on BSE
742 image represent wt. % As.
743
744 **Fig. 11.** Elemental maps generated with LA-ICP-MS which show the distributions of selected trace
745 elements in an oscillatory zoned Py_{2a} crystal from the Qiucun deposit.
746
747 **Fig. 12.** Elemental maps generated with LA-ICP-MS which show the distributions of selected trace
748 elements in Py_2 aggregate in Stage II vein from the Qiucun deposit.
749
750 **Fig. 13.** Histograms showing the distribution of $\delta^{34}S$ values of different generations of pyrite in Stage
751 I (a) and Stage II (b). (c) Log fO_2–pH diagram showing stability relationships in the Fe-O-S system
752 and alteration assemblages for gold mineralization in the Qiucun deposit at 250°C. The diagrams
753 show the predominance boundaries of aqueous sulfur species (pink dashed), mineral stability in the
754 Fe-O-S system (red solid), alteration equilibra (gray solid), and calcite dissolution (black dashed).
755 The sulfur isotope counters are indicated by blue lines (after Ohmoto 1972; Zhai et al. 2020).
756
757 **Fig. 14.** A cartoon illustrating a model for pyrite formation and gold re-enrichment at Qiucun. See
758 text for explanations.
759

760 ## Table Caption

761 **Table 1**
762 Statistic values of LA-ICP-MS analyses of each pyrite generation from the Qiucun gold deposit.
763
764

This is the peer-reviewed, final accepted version for American Mineralogist, published by the Mineralogical Society of America.
The published version is subject to change. Cite as Authors (Year) Title. American Mineralogist, in press.
DOI: https://doi.org/10.2138/am-2022-8030. http://www.minsocam.org/

Table 1

Statistic values of LA-ICP-MS analyses of each pyrite generation from the Qiucun gold deposit.

Pyrite generations	Statistical Parameters	Au	Co	Ni	Cu	Zn	As	Se	Ag	Sb	Te	Hg	Tl	Bi	Pb
Py_{1a}	Min	bdl	bdl	0.81	bdl	bdl	5.9	bdl	bdl	bdl	bdl	bdl	bdl	bdl	bdl
$n = 32$	Max	2.5	590	368	1088	527	5649	8.0	197	293	11	0.96	3.2	31	3969
	Med	0.28	27	26	40	1.5	343	2.3	12	7.0	0.4	0.00	0.04	0.29	149
	MAD	0.22	26	24	39	1.4	323	1.2	10	6.4	0.4	0.00	0.04	0.28	148
Py_{1b}	Min	bdl	bdl	bdl	bdl	bdl	1112	bdl	0.67	bdl	bdl	bdl	bdl	bdl	0.59
$n = 25$	Max	64	212	151	1052	261	32787	9.5	483	7915	5.5	23	620	18	2137
	Med	1.4	12	11	48	1.1	6828	2.4	16	26	0.2	0.07	0.33	0.02	65
	MAD	1.4	11	9.8	42	0.65	5272	1.5	11	24	0.2	0.07	0.32	0.02	57
Py_{2a}	Min	bdl	bdl	bdl	bdl	bdl	109	bdl	bdl	bdl	bdl	bdl	bdl	bdl	bdl
$n = 36$	Max	16	73	107	1362	66	17469	12	1621	4771	45	96	504	2.4	4733
	Med	1.7	4.6	18	42	0.92	3123	1.0	25	77	0.3	0.07	0.89	0.03	66
	MAD	1.5	4.6	18	41	0.67	1890	1.0	22	68	0.3	0.07	0.88	0.02	57
Py_{2b}	Min	1.5	bdl	bdl	bdl	bdl	5851	bdl	6.8	7.7	bdl	bdl	bdl	bdl	5.2
$n = 19$	Max	138	106	55	579	20	21879	7.1	1626	2176	5.5	3.4	188	0.41	389
	Med	31	3.2	3.4	276	1.3	13084	3.1	40	68	0.2	0.03	0.30	0.01	63
	MAD	29	3.2	3.3	182	1.1	2941	0.71	29	39	0.2	0.03	0.22	0.01	36

All data are presented in ppm.

Abbrevations: bdl = below detection limit, Min = minimum value, Max = maximum value, Min = minimum value, MAD = median absolute deviation, *n* = number of analysis.

This is the peer-reviewed, final accepted version for American Mineralogist, published by the Mineralogical Society of America.
The published version is subject to change. Cite as Authors (Year) Title. American Mineralogist, in press.
DOI: https://doi.org/10.2138/am-2022-8030. http://www.minsocam.org/

Fig. 1.

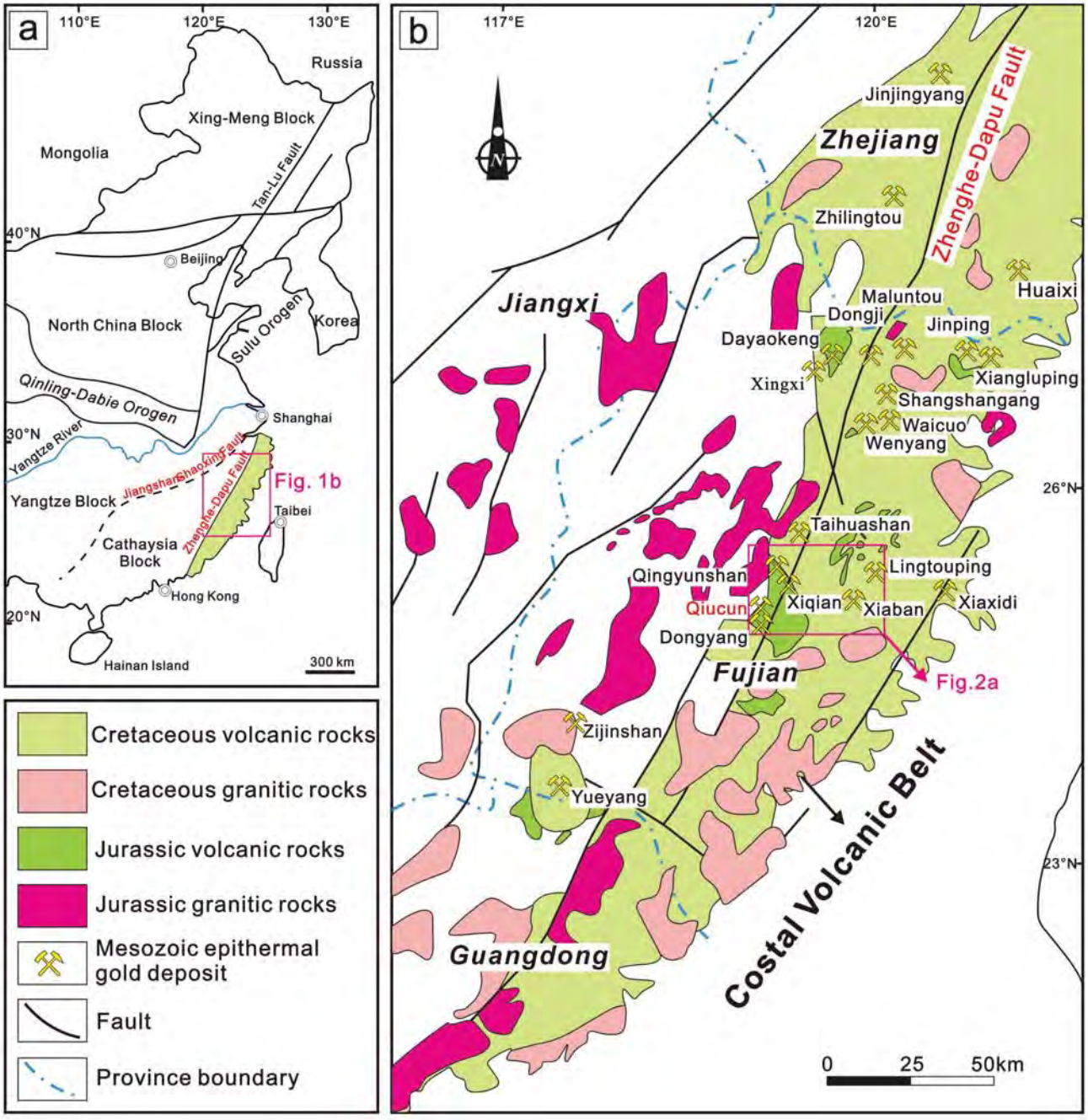

This is the peer-reviewed, final accepted version for American Mineralogist, published by the Mineralogical Society of America.
The published version is subject to change. Cite as Authors (Year) Title. American Mineralogist, in press.
DOI: https://doi.org/10.2138/am-2022-8030. http://www.minsocam.org/

Fig. 2.

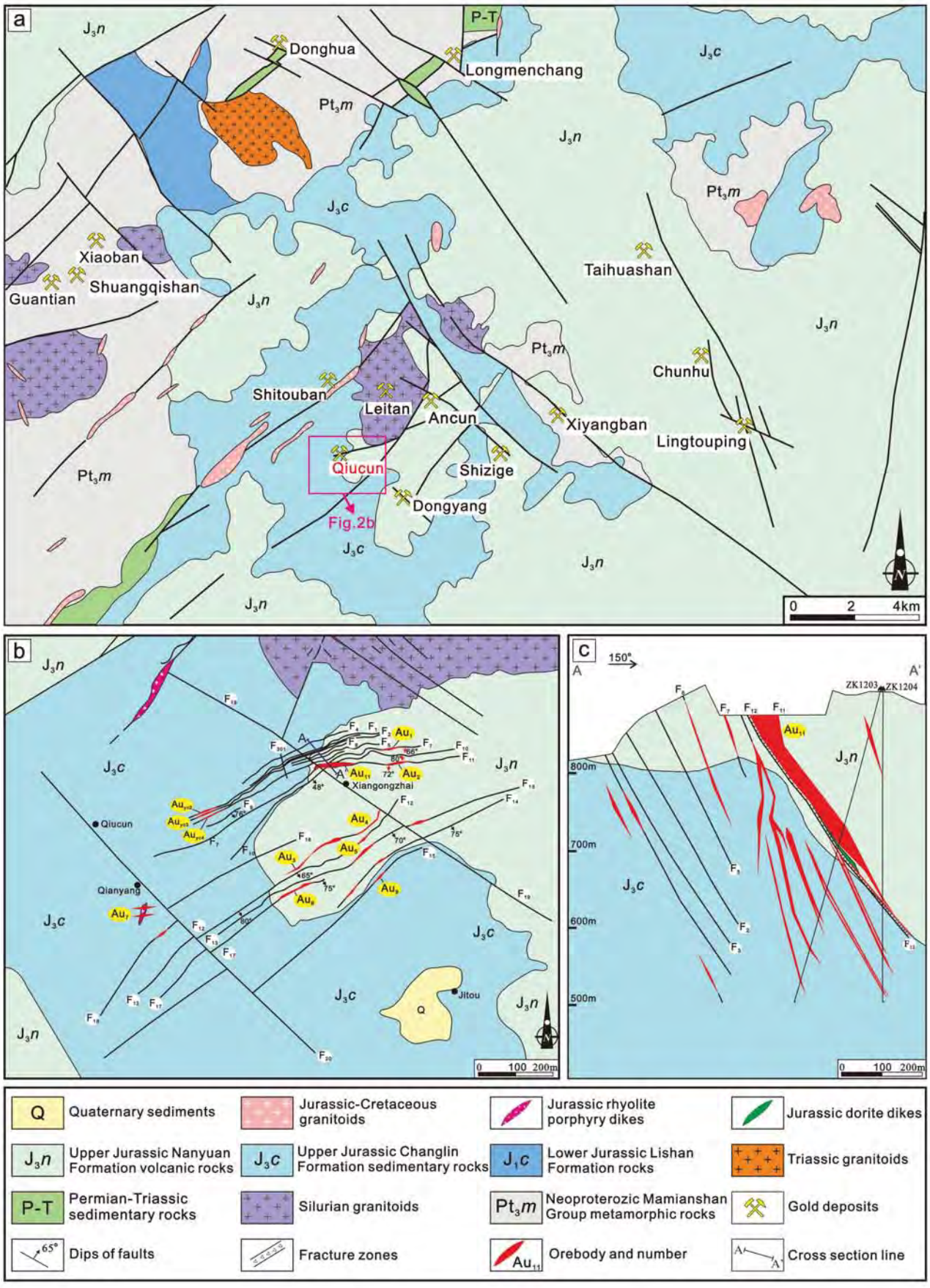

This is the peer-reviewed, final accepted version for American Mineralogist, published by the Mineralogical Society of America.
The published version is subject to change. Cite as Authors (Year) Title. American Mineralogist, in press.
DOI: https://doi.org/10.2138/am-2022-8030. http://www.minsocam.org/

Fig. 3.

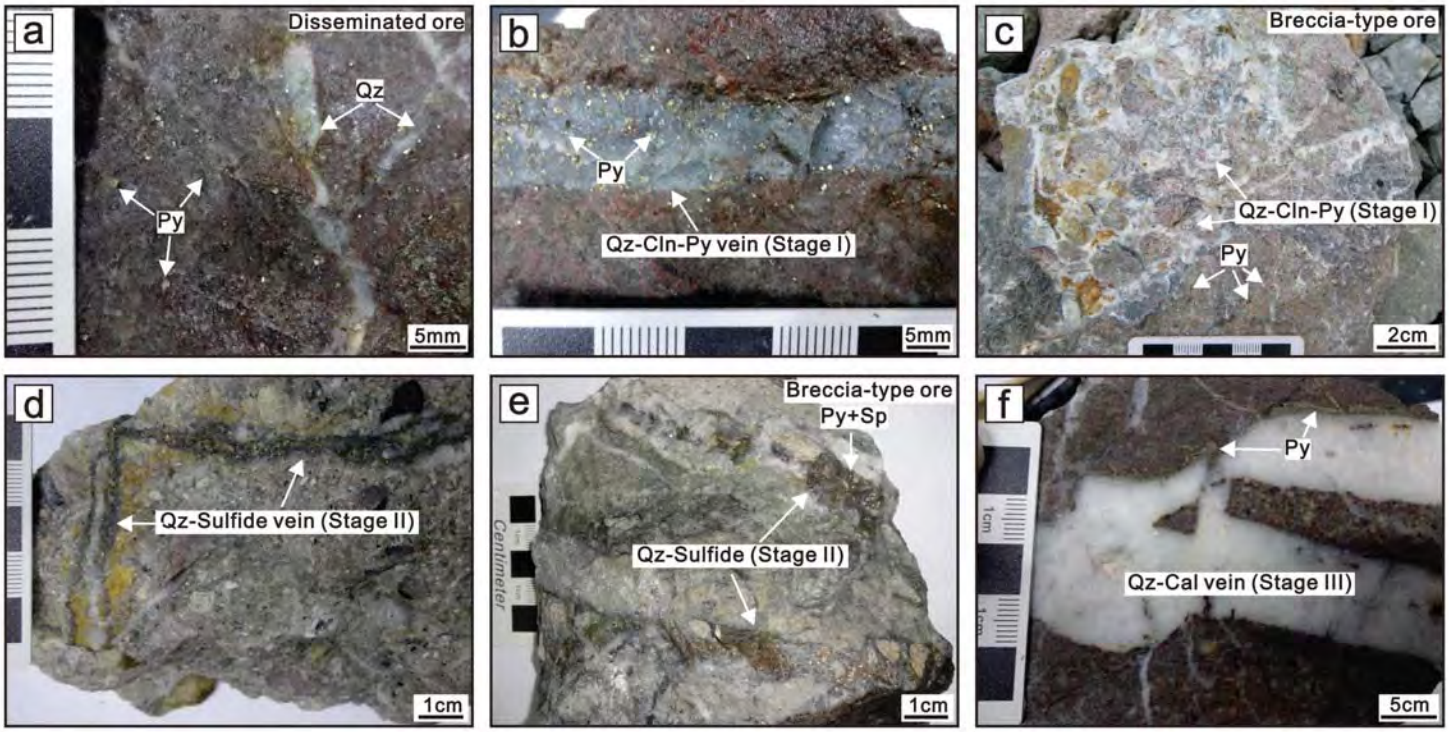

This is the peer-reviewed, final accepted version for American Mineralogist, published by the Mineralogical Society of America.
The published version is subject to change. Cite as Authors (Year) Title. American Mineralogist, in press.
DOI: https://doi.org/10.2138/am-2022-8030. http://www.minsocam.org/

Fig. 4.

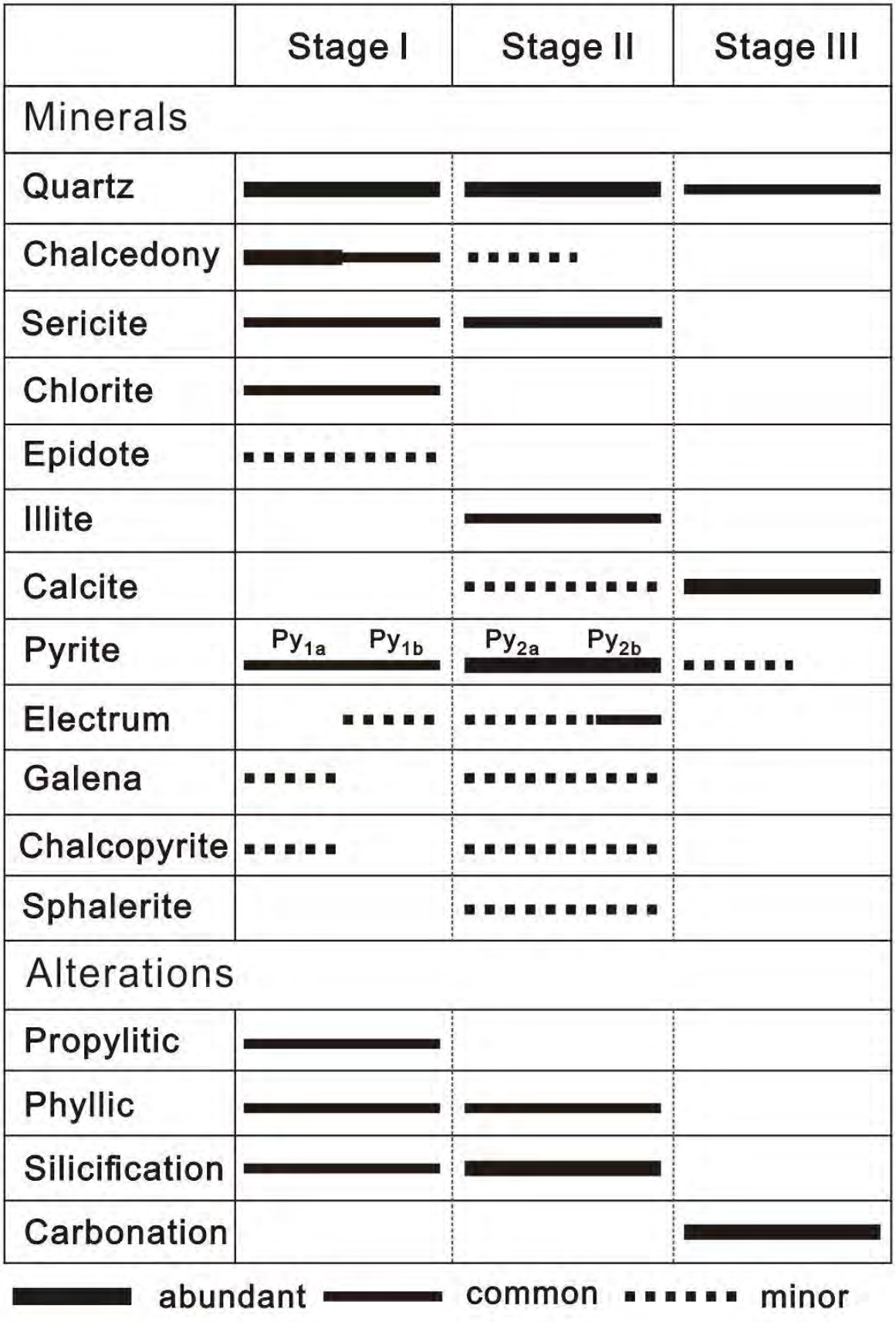

This is the peer-reviewed, final accepted version for American Mineralogist, published by the Mineralogical Society of America.
The published version is subject to change. Cite as Authors (Year) Title. American Mineralogist, in press.
DOI: https://doi.org/10.2138/am-2022-8030. http://www.minsocam.org/

Fig. 5.

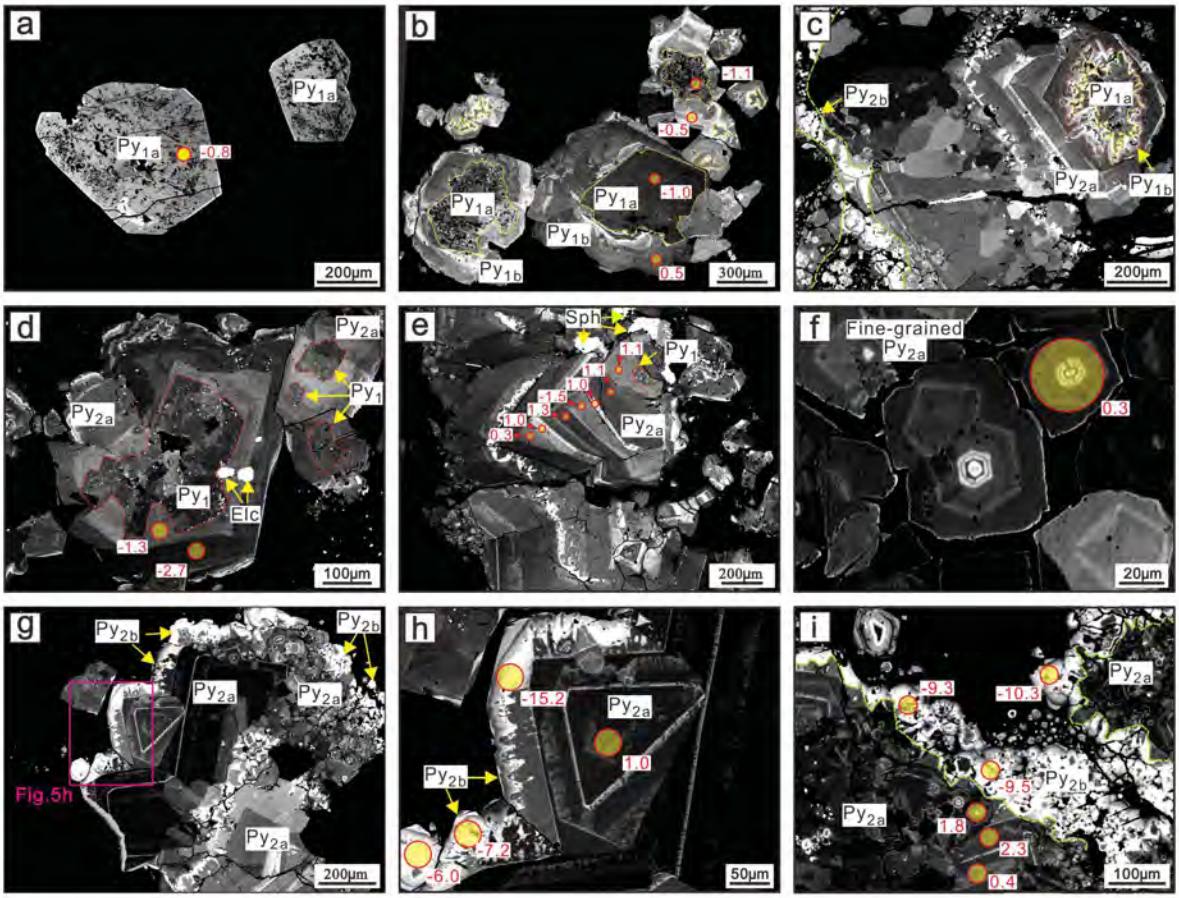

Fig. 6.

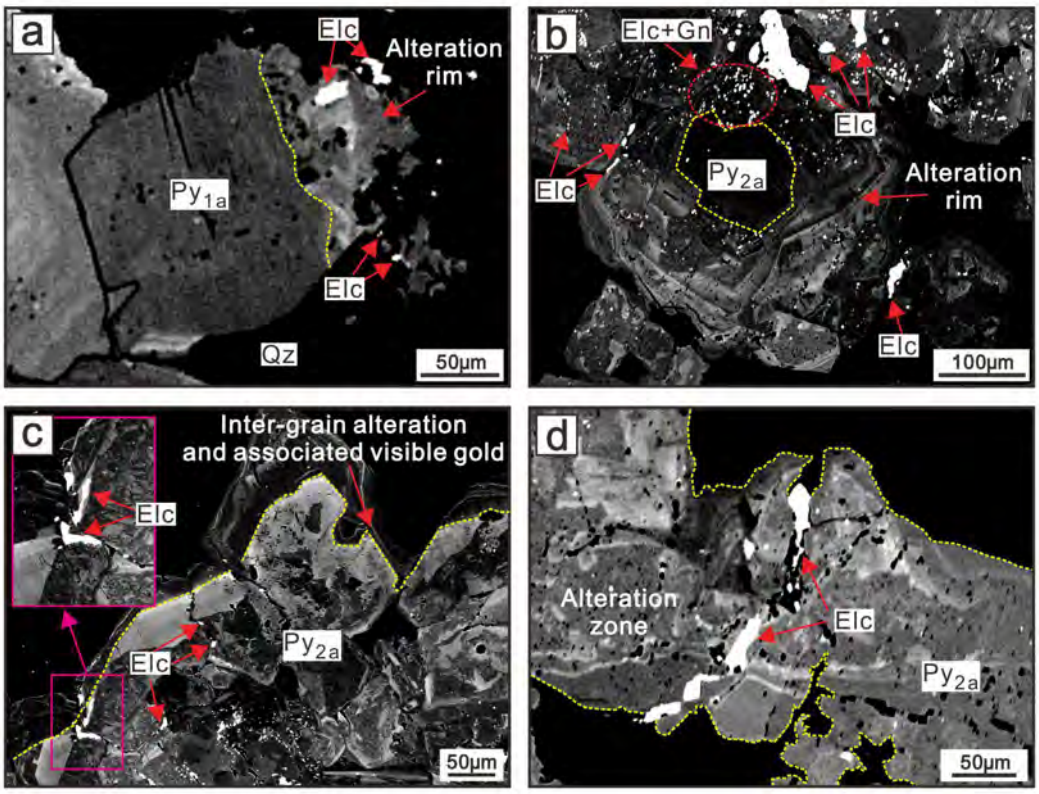

This is the peer-reviewed, final accepted version for American Mineralogist, published by the Mineralogical Society of America.
The published version is subject to change. Cite as Authors (Year) Title. American Mineralogist, in press.
DOI: https://doi.org/10.2138/am-2022-8030. http://www.minsocam.org/

Fig. 7.

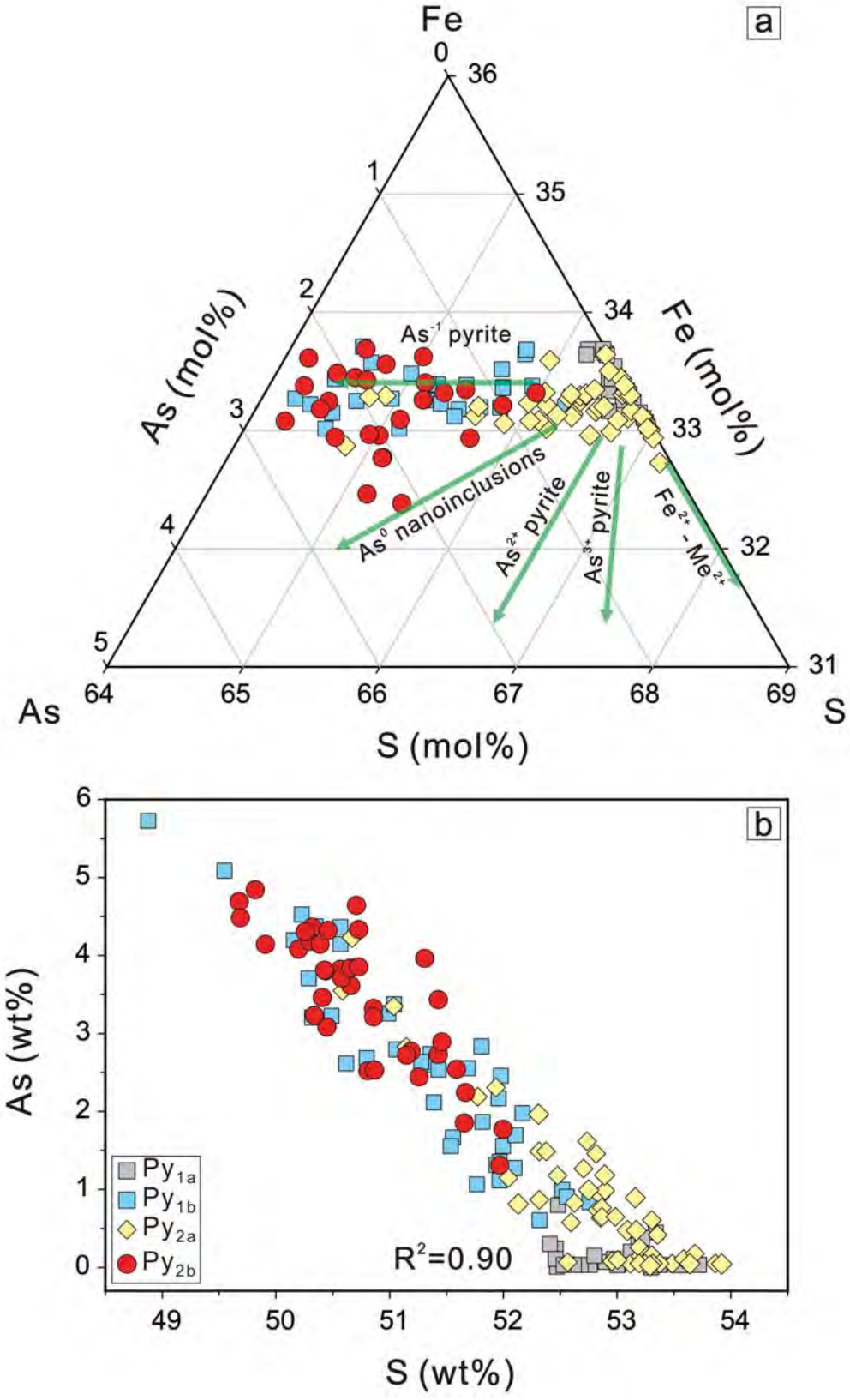

This is the peer-reviewed, final accepted version for American Mineralogist, published by the Mineralogical Society of America.
The published version is subject to change. Cite as Authors (Year) Title. American Mineralogist, in press.
DOI: https://doi.org/10.2138/am-2022-8030. http://www.minsocam.org/

Fig. 8.

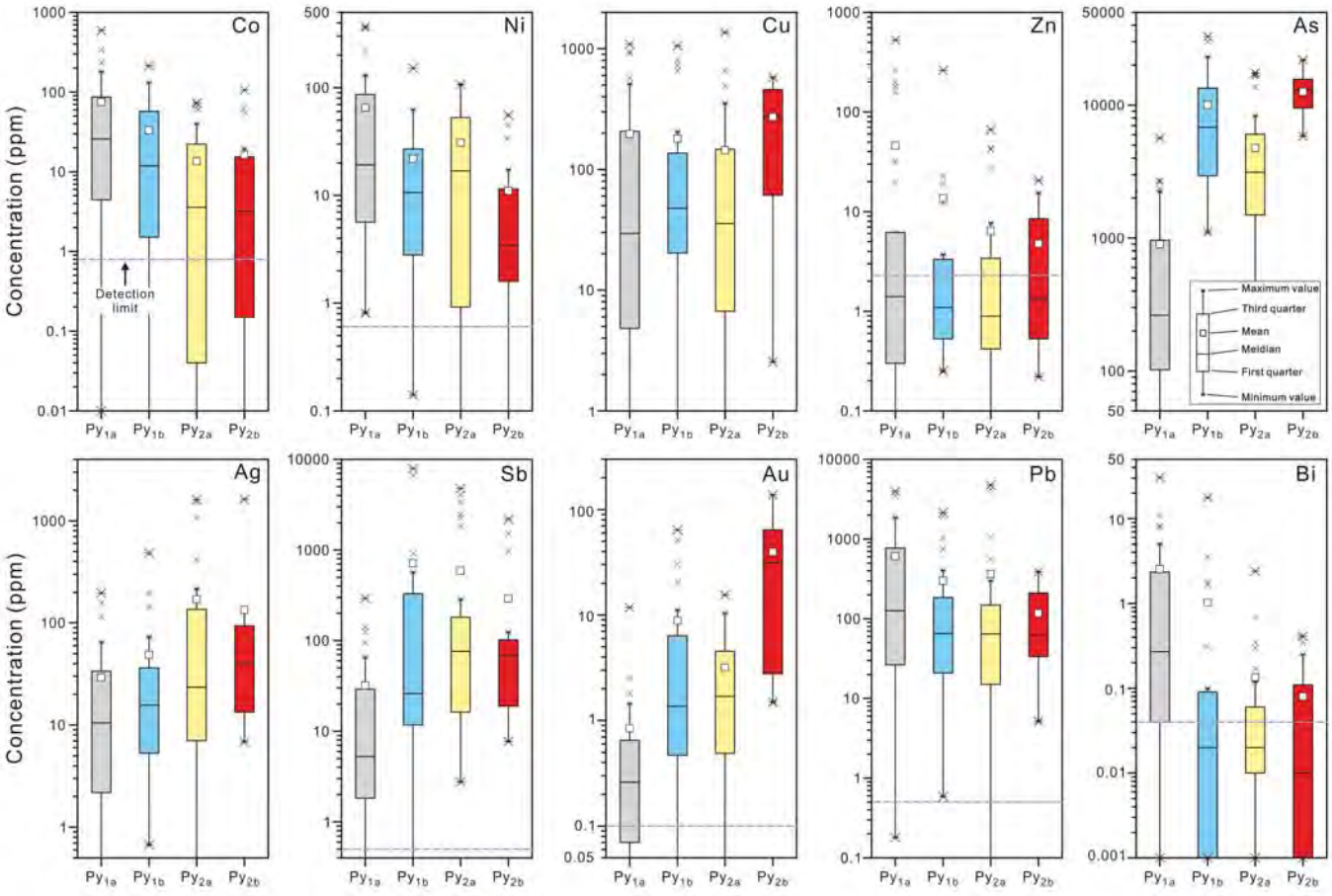

This is the peer-reviewed, final accepted version for American Mineralogist, published by the Mineralogical Society of America.
The published version is subject to change. Cite as Authors (Year) Title. American Mineralogist, in press.
DOI: https://doi.org/10.2138/am-2022-8030. http://www.minsocam.org/

Fig. 9.

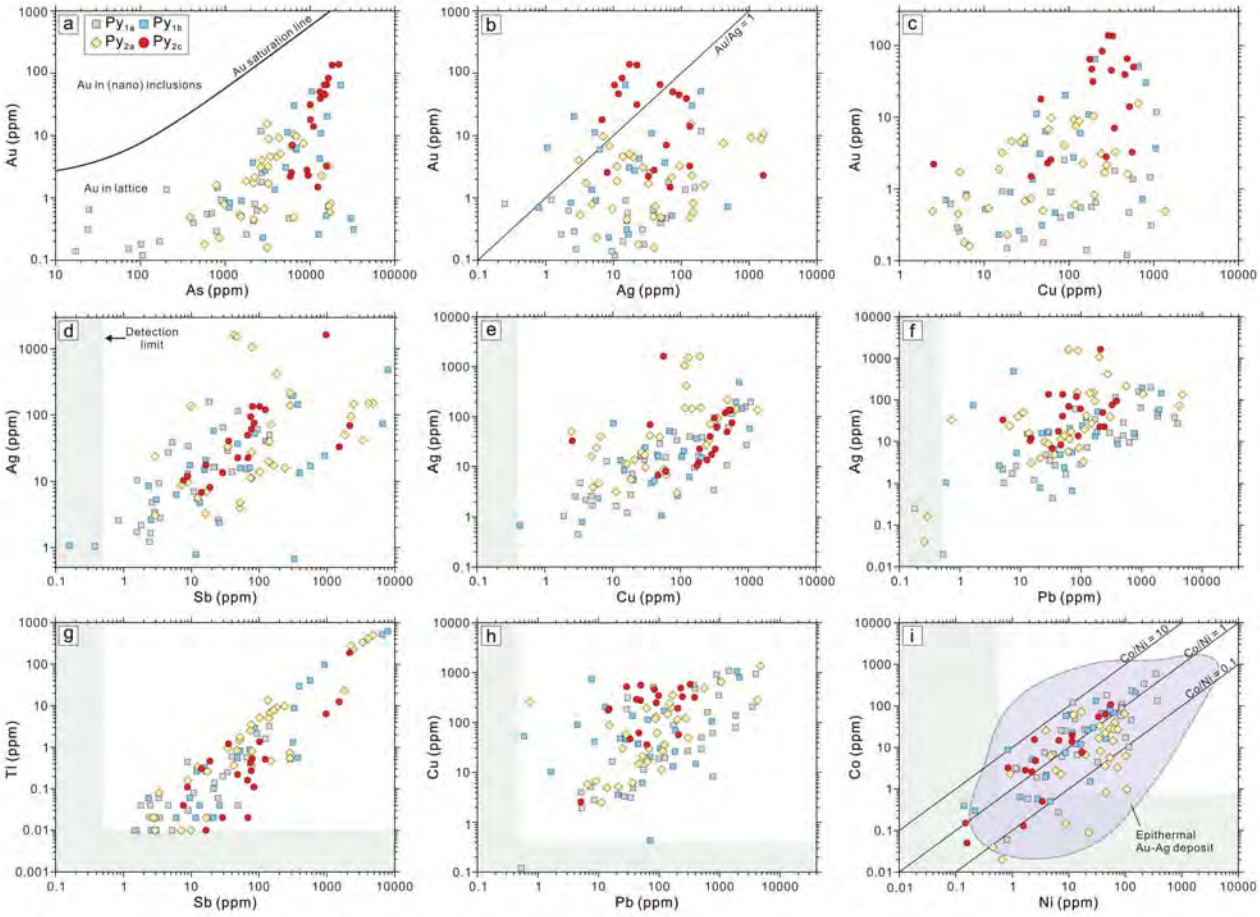

This is the peer-reviewed, final accepted version for American Mineralogist, published by the Mineralogical Society of America.
The published version is subject to change. Cite as Authors (Year) Title. American Mineralogist, in press.
DOI: https://doi.org/10.2138/am-2022-8030. http://www.minsocam.org/

Fig. 10.

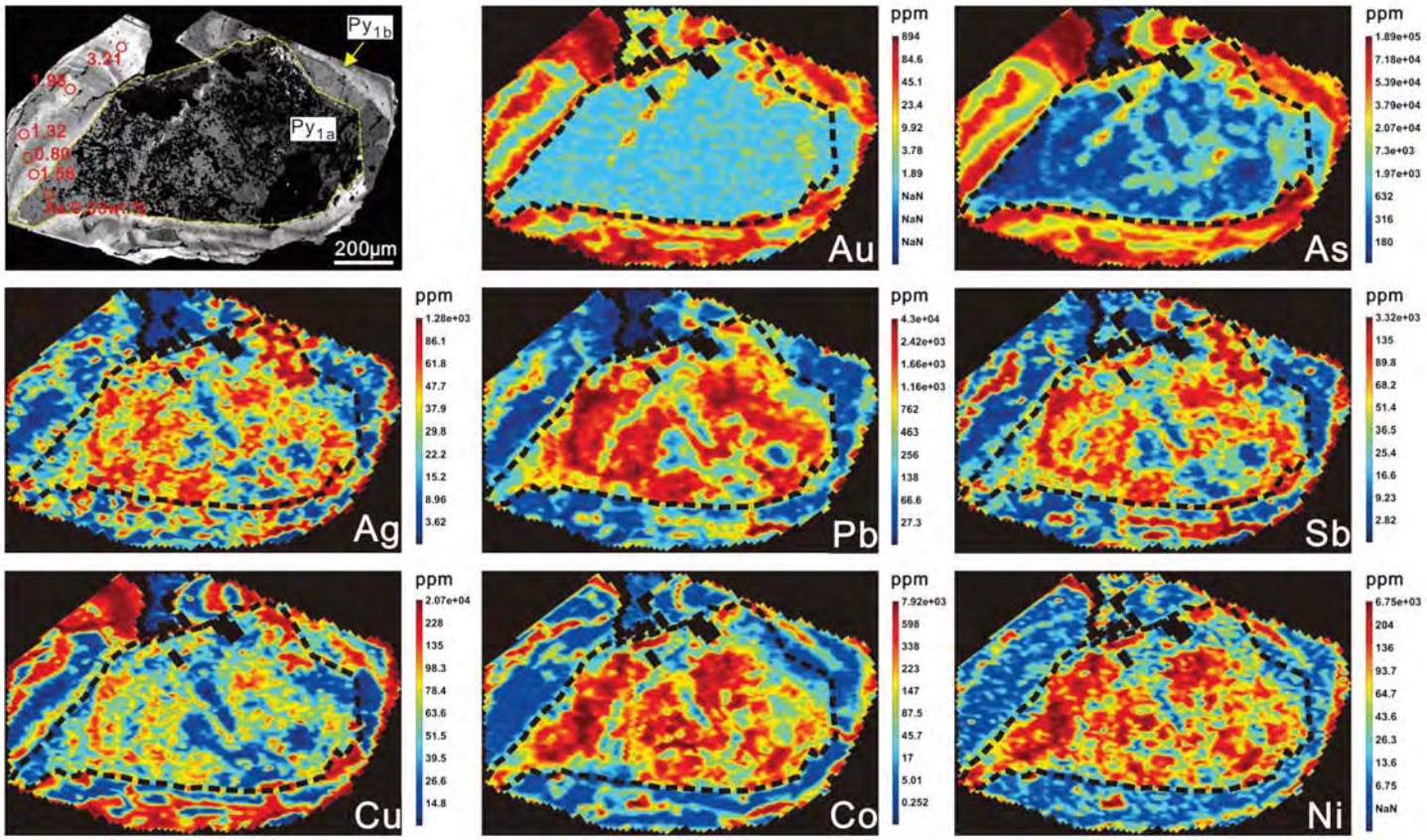

This is the peer-reviewed, final accepted version for American Mineralogist, published by the Mineralogical Society of America.
The published version is subject to change. Cite as Authors (Year) Title. American Mineralogist, in press.
DOI: https://doi.org/10.2138/am-2022-8030. http://www.minsocam.org/

Fig. 11.

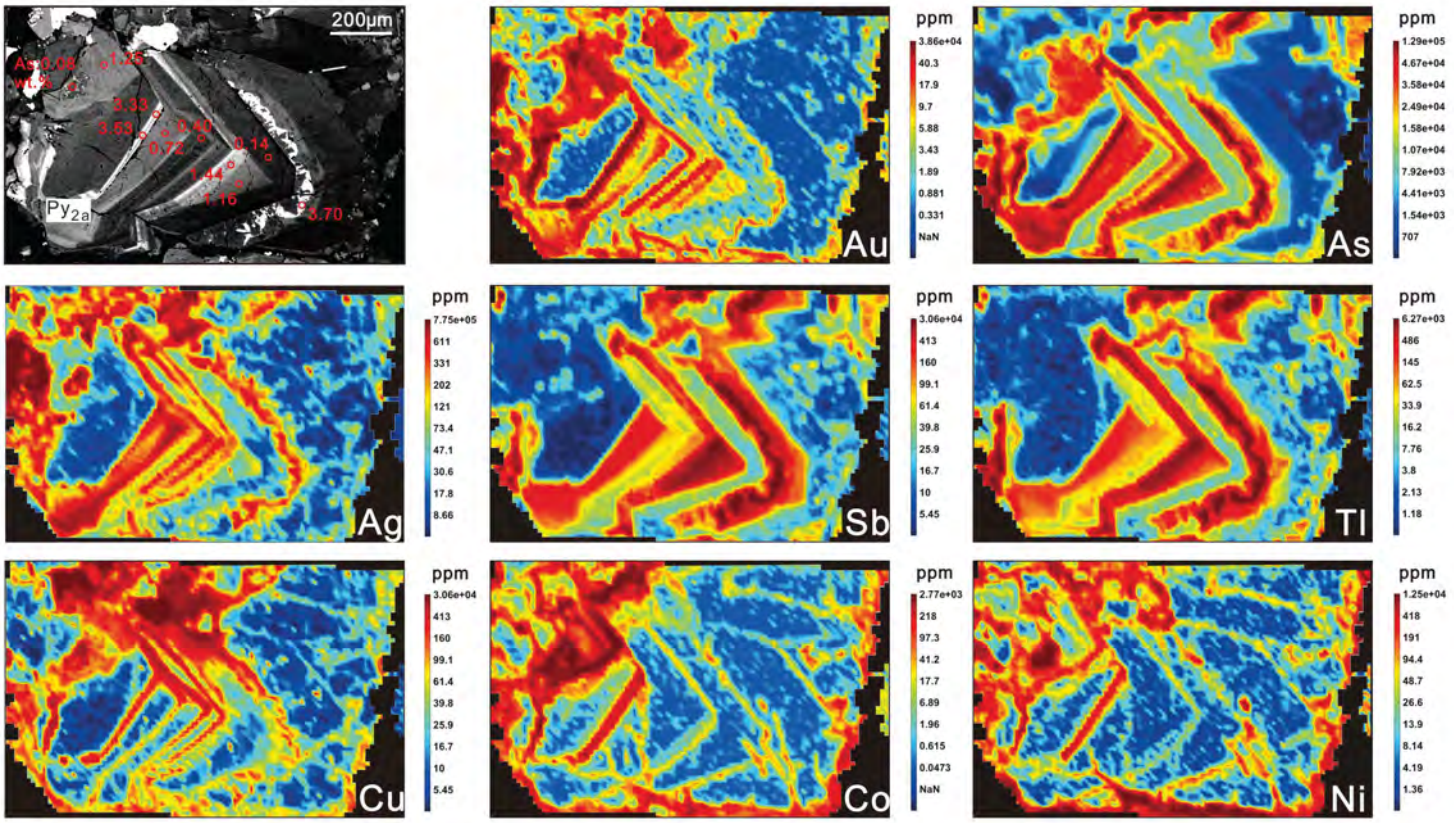

This is the peer-reviewed, final accepted version for American Mineralogist, published by the Mineralogical Society of America.
The published version is subject to change. Cite as Authors (Year) Title. American Mineralogist, in press.
DOI: https://doi.org/10.2138/am-2022-8030. http://www.minsocam.org/

Fig. 12.

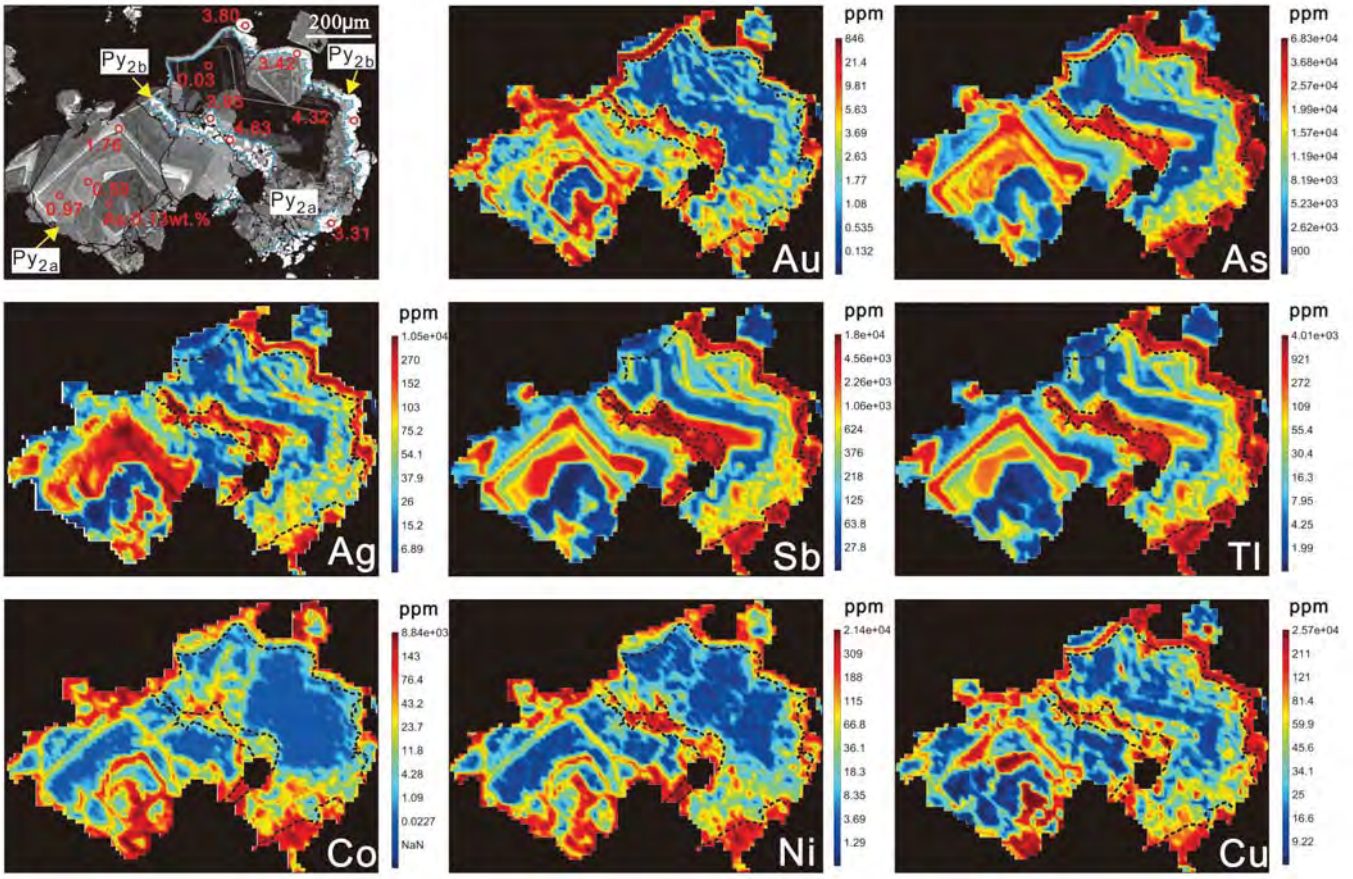

This is the peer-reviewed, final accepted version for American Mineralogist, published by the Mineralogical Society of America.
The published version is subject to change. Cite as Authors (Year) Title. American Mineralogist, in press.
DOI: https://doi.org/10.2138/am-2022-8030. http://www.minsocam.org/

Fig. 13.

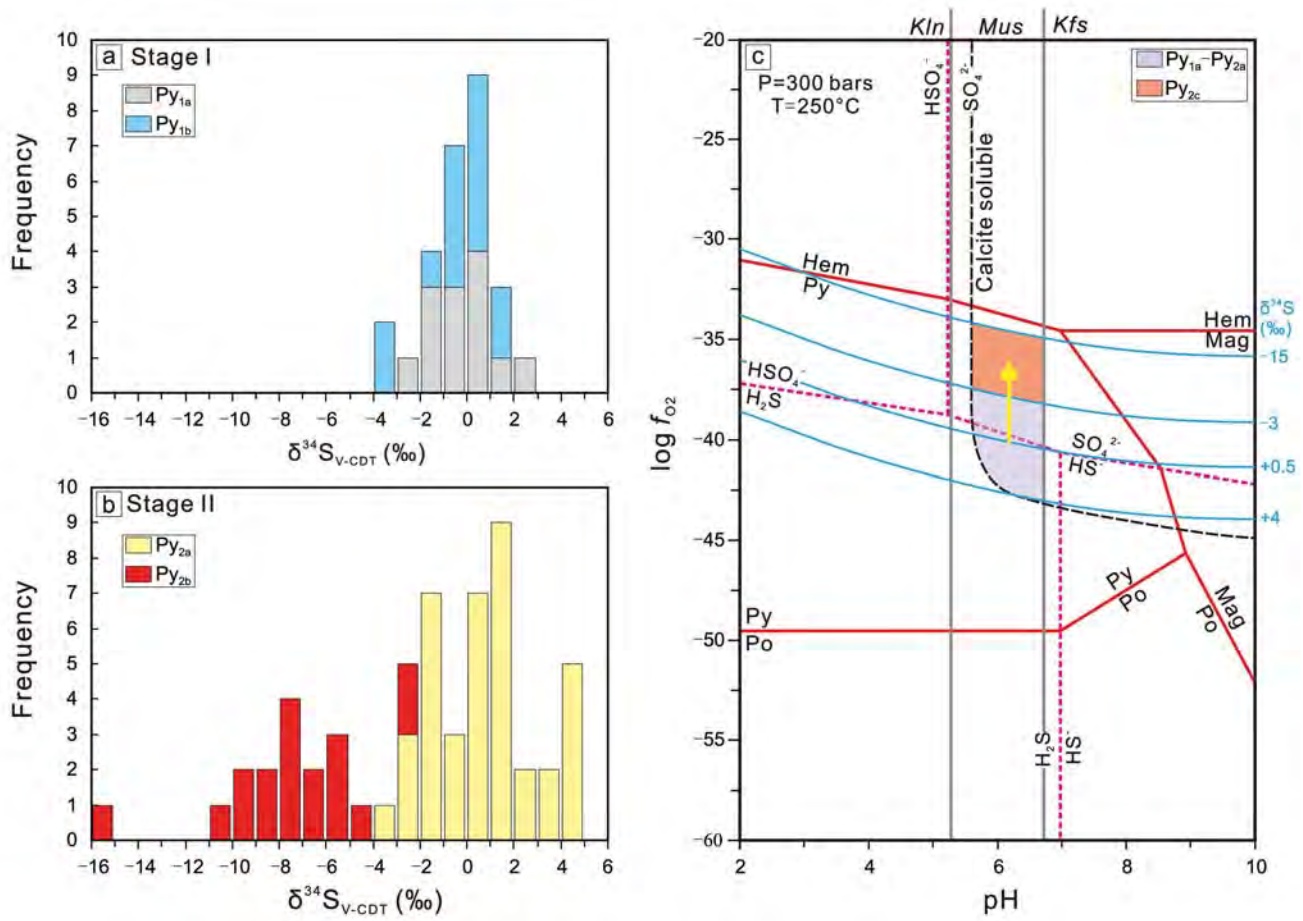

This is the peer-reviewed, final accepted version for American Mineralogist, published by the Mineralogical Society of America.
The published version is subject to change. Cite as Authors (Year) Title. American Mineralogist, in press.
DOI: https://doi.org/10.2138/am-2022-8030. http://www.minsocam.org/

Fig. 14.